JOURNAL OF AIRCRAFT
Vol. 45, No. 4, July–August 2008

Numerical Calculation of Impulsive and Indicial Aerodynamic Responses Using Computational Aerodynamics Techniques

Alexandre Noll Marques*
Instituto Tecnológico de Aeronáutica, 12228-900 São José dos Campos, Brazil
and
João Luiz F. Azevedo†
Instituto de Aeronáutica e Espaço 12228-903 São José dos Campos, Brazil

DOI: 10.2514/1.32151

The present work presents a detailed study on the numerical calculation of impulsive and indicial unsteady aerodynamic responses with modern computational fluid dynamics solvers. A brief historical background on this subject is presented, and it is shown how new interpretations of computational fluid dynamics solvers as discrete-time systems change the way impulsive and indicial responses can be directly obtained. The objective is to demonstrate that the rigorous relationships theoretically established among the aerodynamic responses to impulse, indicial, harmonic, and smooth inputs can be numerically reproduced with modern computational fluid dynamics solvers. Although the numerical results presented herein are obtained with a single computational fluid dynamics tool, the argument is valid, in principle, for all numerical solution schemes. The computational fluid dynamics tool in question solves the two-dimensional Euler equations with an explicit time march, using a finite volume discretization which supports fully unstructured grids. The results are compared both in the time and in the frequency domains, which yields a more complete understanding of details of the numerical solutions.

I. Introduction

INDICIAL and impulsive responses are essential to the determination of the dynamic characteristics of any system. In the aerodynamic case, such responses are important to the fields of flight control and stability, aeroelasticity, and aeroservoelasticity, just to name a few. Traditionally, the methods developed for determining the unsteady aerodynamic behavior for subsonic and supersonic regimes are based on linearized formulations [1,2], which do not present the same satisfactory results in the transonic range. According to Tijdeman [3], this occurs due to the nonlinearity of transonic flows characterizing a significant alteration of the flow behavior, even when a profile is submitted to small perturbations. Along the last three decades, at least, there have been many attempts to numerically solve more elaborate aerodynamic models for the unsteady transonic regime. Beam and Warming [4] presented one of the earliest papers on solving the unsteady Euler equations. They used an explicit, third-order, noncentered, finite difference scheme to obtain indicial solutions for plunging flat plates and parabolic arc airfoils in the transonic regime. However, the boundary conditions were imposed in a small-disturbance fashion on a mean-surface approximation to the thick airfoil. This procedure was not considered satisfactory for more practical airfoils. This fact, together with memory and computational time limitations, led to the development of numerical solvers based on the nonlinear transonic potential formulations. Traci et al. [5] developed the STRANS2 and UTRANS2 codes to solve the transonic steady and unsteady equations by the relaxation method. The unsteady equation is time linearized by treating the unsteady solution as a small linear harmonic perturbation about a nonlinear steady-state solution. This approach has the obvious drawback of not being able to represent solutions to indicial excitations, only to harmonic ones. Later, Ballhaus and Goorjian [6] developed the LTRANS2 code to time accurately solve the low-frequency transonic small disturbance (TSD) formulation. This formulation is able to capture small shock motions. Yang et al. [7] present a compilation of the results obtained with the application of these and other transonic codes to different cases of aeroelastic analyses. Ashley [8] reported the use of semi-empirical corrections to linearized theory results as a means of improving flutter predictions. Nevertheless, Ashley [8] himself believed that really satisfactory aeroelastic quantitative predictions of the transonic regime should be possible only when accurate, three-dimensional, unsteady computational fluid dynamics codes were developed.

Computational fluid dynamics (CFD) is a subject that has played an extremely important role in recent aerodynamic studies. The possibility of numerically treating a broad range of phenomena that occur in flows over bodies of practically any geometry has numerous advantages over experimental determinations, such as greater flexibility together with time and financial resource savings. However, obtaining more reliable numerical results for a growing number of situations has been one of the major recent challenges in many science fields. Hirsch [9] shows that, particularly in aerodynamics, the general phenomena are governed by the Navier–Stokes equations, which constitute a system of coupled nonlinear partial differential equations that has no general analytical solution. He also comments, among other issues concerning CFD techniques, on how to simplify the mathematical models conveniently to ease the numerical treatment of each case. Space and time discretization schemes, as well as convergence acceleration techniques, boundary condition establishment, and other numerical integration tools, are available and largely used to solve such models.

Nevertheless, the use of indicial and impulse excitations with more complex CFD solvers has led to some misinterpretations in the beginning of the 1990s. Time-marching schemes possess the ability to solve perturbations, which advance through the flowfield with velocities up to some determined limit. This limit depends on the scheme itself and on the mesh resolution [9]. Consequently, care must be taken when evaluating indicial and impulsive responses with CFD codes because such excitations usually cause large perturbation

Presented as Paper 4067 at the 25th AIAA Applied Aerodynamics Conference, Miami, FL, 25–28 June 2007; received 14 May 2007; revision received 16 January 2008; accepted for publication 18 January 2008.

*Master of Science Student, Division of Aeronautical Engineering, Comando-Geral de Tecnologia Aeroespacial; ale_noll@yahoo.com. Student Member AIAA.

†Senior Research Engineer, Aerodynamics Division, Comando-Geral de Tecnologia Aeroespacial; azevedo@iae.cta.br. Associate Fellow AIAA.

velocities. This is very well illustrated in [4,6] for simpler codes, and more recently in [10] for more sophisticated and modern solvers. But, despite the difficulties in dealing with these velocities, they are finite in magnitude, opposite to what [11] has stated. This misinterpretation is easily understood in light of the usual definition of the impulse and indicial, or step, functions in which a discontinuous change of the function value causes an indefinite derivative. This indefinite value is many times considered infinite, what, consequently, leads to infinite velocities. Actually, although the terminology "impulse function" is used throughout this paper, it should be noted that it is not rigorously a function, but rather a "generalized function" [12], and that the derivative of both the impulse and indicial functions becomes mathematically consistent only in certain integral applications.

Hence, the numerical implementation of such discontinuous functions can be quite controversial, and some authors even state that such implementation is not feasible [13]. However, recently Silva [14] showed that, once the flow governing equations are discretized, the resultant system can no longer be viewed as a continuous-time system, but it should be treated as a discrete-time system. Furthermore, linear discrete-time systems present properties that are very similar to those of linear continuous-time systems and, more important, the convolution theorem is valid [15]. Therefore, as explained later, there are discrete-time sequences that, when applied as input to discrete-time systems, possess the exact same properties of the impulse and indicial functions. Their definitions are quite different from the corresponding continuous functions. Namely, they do not contain any singularities, and their numerical implementation is straightforward. In fact, although they are well-defined sequences for discrete-time systems, and they are by no means mere approximations of continuous functions, these sequences have been used as approximations of the impulse and step excitations in many numerical applications over the years [4,6]. Hence, the new interpretation proposed by Silva [14] comes to validate and reaffirm as a rigorous procedure what was thought to be an approximation until recently.

The difficulties of treating the high velocities induced by the impulse and indicial excitations can be overcome by the use of smoother excitations [11,13,16]. Although such smooth excitations do not possess all the characteristics of the impulse and indicial ones, neither is capable of uniformly exciting the entire frequency domain; they can be calibrated to excite certain frequency ranges of interest. For aeroelastic purposes, for example, only low reduced frequencies are relevant. The convolution sum [15,17] establishes a relationship between the desired impulsive response and the one actually obtained with the smooth excitations for the frequency range of interest.

The authors believe that they are able to present a unified view of the different approaches for obtaining impulsive and indicial aerodynamic responses through the application of modern CFD solvers. In fact, this unified view should demonstrate that these different approaches are rigorously equivalent and, when correctly implemented, generate identical results within the numerical accuracy expected from any numerical method. Actually, the present work is based on the finite volume formulation in which a CFD tool is applied with two-dimensional unstructured meshes around lifting surfaces to acquire unsteady responses to harmonic, smooth pulse, discrete step, and unit sample motions. The unit sample sequence is defined later as the discrete-time sequence equivalent to the continuous-time impulse function. Although this investigation is conducted with a particular CFD solver, it is believed that the results presented here are representative of most numerical schemes used in modern CFD solvers.

The development of the CFD tool applied in the present work is a result of the increased demand for aerodynamic parameters that followed the evolution of the work and projects performed by Instituto de Aeronáutica e Espaço (CTA/IAE). Nevertheless, the application of CFD tools in these parametric analyses has always been limited by the need of adequate code development and the lack of computational resources compatible with the work to be performed. Therefore, a progressive approach has been adopted in the development of CFD tools in CTA/IAE and in Instituto Tecnológico de Aeronáutrica (ITA), as presented in [13,17–24].

II. Continuous-Time Impulsive and Indicial Responses

Linear time-invariant continuous-time systems present the very interesting property of possessing elementary solutions that are representative of the entire frequency content of the system response. The most elementary solution is the impulsive one [25]. This is evident from the fact that every other continuous input can be seen as the integration of successive time-shifted and scaled impulse excitations. Hence, as a consequence of the superposition principle, the corresponding result is the integration of the responses to each of these impulses, scaled by the input magnitude. This results in the convolution integral of the impulsive response with the given input. In a frequency domain point of view, the Fourier transform of an impulse function assumes a unit value over the entire domain. In other words, an impulse input has the capability of uniformly exciting a system in the entire frequency domain.

Similarly, the step, or indicial, response is another elementary solution. Ballhaus and Goorjian [6] develop a graphical and intuitive demonstration of how a series of time-shifted and scaled step functions are equivalent to any continuous function. Therefore, just as reasoned before, the convolution integral of the indicial response, but at this time with the input time derivative, is equal to the system response to that particular excitation. This convolution integral is called the Duhamel integral.

Therefore, the determination of the impulsive or indicial response of an aerodynamic system is sufficient to know all the unsteady behavior of that system. Such approach is very interesting for engineering situations in which the aerodynamic behavior is coupled with other dynamic systems such as in aeroelasticity and aeroservoelasticity. By doing so in the aeroelastic problem, for example, the governing equations of the structural dynamic problem may be solved separately from the aerodynamic equations. In this case, the aerodynamic influence is represented in terms of the aerodynamic forces, which, in turn, are known for an arbitrary deformation of the structure [1,13]. The linearity hypothesis may seem too constraining, because the use of complex CFD solvers is justified in highly nonlinear problems. However, as shown in the results section, there is an amplitude range in which the aerodynamic response due to the unsteady motion can be considered linear with respect to the mode shapes, even in the transonic regime. Moreover, there are applications in which this linear range is of interest. Using the aeroelastic problem as an example once again, the linear responses can be used for the determination of the flutter onset point [17]. This means that the point in which the small oscillations start to diverge can be identified. There may be cases in which the nonlinear effects restrain this divergent motion, creating limit cycle oscillations, for instance, and such situations may not be predicted due to the linear assumption. However, for safety reasons, the flutter onset is very important to designers.

Furthermore, the impulse and step functions are conceptually correct in a continuous-time context, and they present discontinuities that cannot be implemented in numerical codes. The proper process of obtaining elementary solutions with CFD solvers, and also interpreting such solutions, requires a rather different approach, which is the subject discussed in the next section.

III. CFD Solver as a Discrete-Time System

As aeronautical researchers are generally used to dealing with continuous-time problems, it has been very common in the literature to look at CFD solvers as mere approximations to continuous-time systems. Therefore, it is equally common to use continuous-time system properties and thinking when performing CFD simulations, as seen in [4,6,11,13,16,26–28]. They are approximations, indeed, but discrete-time approximations. Hence, as shown by Silva [14], once the governing equations have been discretized, the resulting numerical scheme is actually a discrete-time system, which has its own properties and peculiarities.

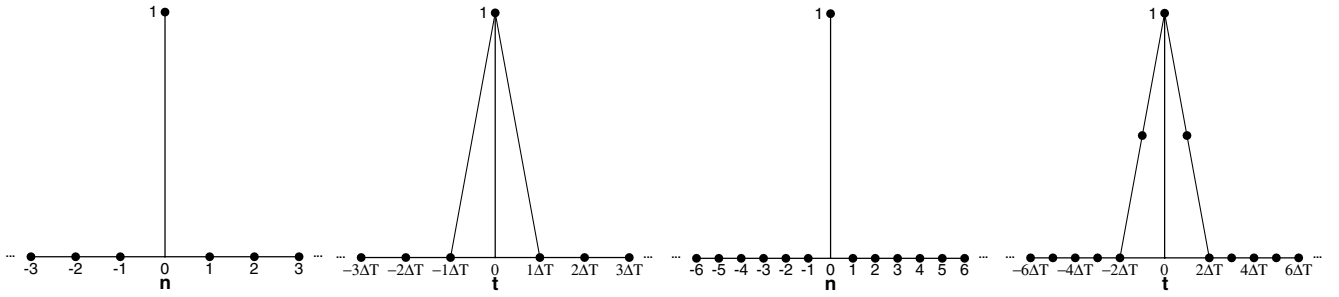

a) Unit sample sequence **b) Sampled triangular function** **c) Unit sample sequence with half the time step** **d) Sampled triangular function with half the time step**

Fig. 1 Differences between a unit sample sequence and a sampled function.

This misinterpretation has led many authors [11,13,16,26] to justify the use of smooth pulse excitations because the theoretical continuous-time impulse and indicial excitations are not numerically feasible. Nevertheless, Silva [14] has suggested the use of equivalent discrete-time excitations: unit sample and discrete step [15]. The unit sample sequence is given by

$$\delta[n] = \begin{cases} 0, & n \neq 0 \\ 1, & n = 0 \end{cases} \tag{1}$$

and the discrete step sequence is

$$u[n] = \begin{cases} 0, & n < 0 \\ 1, & n \geq 0 \end{cases} \tag{2}$$

or, equivalently,

$$u[n] = \sum_{i=-\infty}^{n} \delta[i] = \sum_{i=0}^{\infty} \delta[n-i] \tag{3}$$

Special attention must be paid not to confuse the unit sample with a sampled version of a triangular continuous-time function. Figure 1 is an example of how different these can be. Figure 1a shows a standard unit sample sequence, and Fig. 1b a continuous triangular function with the corresponding samples. At first, both the sampled function and the unit sample sequence are identical. But now consider the same function sampled with a different time step, half of the original one. This situation is represented in Fig. 1d. However, the unit sample sequence input does not depend on the time step, as demonstrated in Fig. 1c, which is exactly the same as Fig. 1a but with a different horizontal axis scale.

The unit sample and discrete step sequences formally hold properties very similar to the ones attributed to the impulse and step functions, respectively. Namely, if a linear time-invariant discrete-time system is subjected to a unit sample excitation, then the corresponding response will contain all the information about the system, and the response to every other input is given by the convolution sum [15]

$$\text{out}[n] = \text{in}[n] \cdot h[n] = \sum_{i=-\infty}^{\infty} \text{in}[i]h[n-i] = \sum_{i=-\infty}^{\infty} \text{in}[n-i]h[n] \tag{4}$$

where in$[n]$ is a generic input sequence, out$[n]$ is the respective response, and $h[n]$ is the system response to a unit sample input. It is very important to emphasize that, although the convolution sum given in Eq. (4) resembles the convolution integral [25], it is not an approximation to such integral, but a formally defined discrete operation. Moreover, the unit sample rigorously excites uniformly the complete frequency domain.

The discrete step response also characterizes a discrete-time system because one can reproduce the unit sample response from it [17]. As demonstrated in [17], the backward difference of the discrete step response yields the unit sample one, that is,

$$S[n] - S[n-1] = h[n] \tag{5}$$

where $S[n]$ designates the system response to a discrete step input. Thus, theoretically, it would be more convenient, and even computationally cheaper, because the transient solution should die out more rapidly, to acquire CFD results submitting the body to either unit sample or discrete step type perturbations than to smooth inputs. As mentioned earlier, this has been accomplished by some authors [4,6,10,14,29], but some numerical complications may arise when simulating such cases. Raveh [10], particularly, has performed a thorough inspection of these responses and concluded that numerical errors may occur due to the large velocities induced by sharp motions; when these exceed the propagation velocity, the numerical time-marching scheme can resolve. Naturally, it all depends on the numerical formulation used in the CFD solver, input amplitude, and time step. Additionally, Raveh [10] states that simulations carried out with the discrete step excitation tend to be less influenced by the simulation parameters than those using the unit sample.

All this reasoning does not invalidate the use of smooth excitations, although it changes the way they are understood. This is because they should be seen as discrete input sequences derived from sampling the corresponding continuous functions. However, it is clear that, in face of these new proposals, the authors are interested in evaluating their usage with the present CFD solver, and also in comparing results and efficiency. Such discussions are presented in the results part of the paper. The smooth input used here is the one suggested in [11], which is defined as

$$f_p(t) = \begin{cases} 4\left(\frac{t}{t_{\max}}\right)^2 \exp\left(2 - \frac{1}{1-\frac{t}{t_{\max}}}\right), & 0 \leq t < t_{\max} \\ 0, & t \geq t_{\max} \end{cases} \tag{6}$$

where $t_{\max}$ is the excitation duration. As shown in Fig. 2, the function defined in Eq. (6) guarantees a smooth motion, and both the function and its first derivative go to zero when $t = 0$ and $t = t_{\max}$.

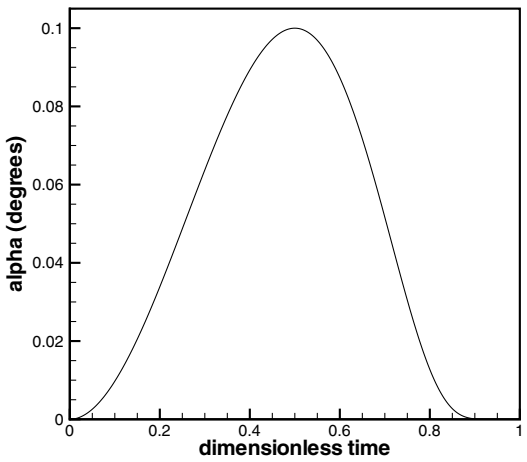

Fig. 2 Exponentially shaped pulse excitation in angle of attack.

As the exponentially shaped input is not a unit sample excitation, the real unit sample response is evaluated using a well-known property of the convolution theorem [15]:

$$g[n] = f_p[n] \cdot h[n] \longrightarrow G[n] = F_p[n]H[n] \tag{7}$$

$$H[n] = \frac{G[n]}{F_p[n]} \tag{8}$$

where $h[n]$ represents the time response to a unit sample excitation, and $g[n]$ is the response to the sampled exponentially shaped excitation $f_p[n]$. The sequences in capital letters are the discrete Fourier transforms of the corresponding sequences in lowercase letters. Therefore, the frequency domain unit sample responses can be obtained by dividing the discrete Fourier transform (DFT) of the responses to the sampled exponentially shaped pulse by the DFT of the input sequence. Although the input is not the exact unit sample excitation, it is capable of exciting the reduced frequencies of interest in aeroelastic studies. The corresponding frequency domain points resulting from this procedure are [13]

$$f[n] = \frac{1}{\Delta t}\frac{n}{N} = \frac{a_\infty}{\Delta \bar{t} c}\frac{n}{N}, \qquad n = 0, 1, 2, \ldots, N_{\max} \tag{9}$$

$$N\max = \begin{cases} N/2, & \text{if } N \text{ is even} \\ (N-1)/2, & \text{otherwise} \end{cases} \tag{10}$$

Here, f designates the frequency, a_∞ is the undisturbed flow sound speed, c is the chord length, Δt is the time step of the aerodynamic solution, and N is the maximum number of discrete iterations in which this solution is known. Moreover, the bar designates a dimensionless time step defined as

$$\Delta \bar{t} = \Delta t \frac{a_\infty}{c} \tag{11}$$

Equation (9), rewritten in terms of the reduced frequency based on the half-chord length (b), stands as

$$\kappa = \frac{\omega b}{U_\infty} = \frac{2\pi f b}{U_\infty} \tag{12}$$

$$\kappa[n] = \frac{\pi}{M_\infty \Delta \bar{t}}\frac{n}{N}; \qquad i = 0, 1, 2, \ldots, N_{\max} \tag{13}$$

where ω is the circular frequency, U_∞ is the undisturbed flow speed, and M_∞ is the undisturbed flow Mach number. Finally, the time domain response results from the inverse discrete Fourier transform [15] of the frequency domain response obtained with the preceding procedure. However, this time domain response is not exactly identical to the unit sample response, because only part of the frequency domain content is properly solved.

IV. Flow Solver

A. Theoretical Formulation

The CFD tool applied in this work is based on the 2-D Euler equations, which represent two-dimensional, compressible, rotational, inviscid, and nonlinear flows. Therefore, it is completely capable of capturing the shock waves present in transonic flows. Because of the use of unstructured meshes and the adoption of the finite volume approach, these equations are written in Cartesian form. Furthermore, as usual in CFD applications, flux vectors are employed and the equations are nondimensionalized. Hence, they can be written as

$$\frac{\partial}{\partial t}\iint_\Omega Q \,\mathrm{d}x\,\mathrm{d}y + \int_S (E\,\mathrm{d}y - F\,\mathrm{d}x) = 0 \tag{14}$$

In Eq. (14), Ω represents the volume of the control volume or, more precisely, its area in the two-dimensional case. S is its surface, or its side edges in 2-D. Q is the vector of conserved properties of the flow, given by

$$Q = [\,\rho \quad \rho u \quad \rho v \quad e\,]^T \tag{15}$$

E and F are the inviscid flux vectors in the x and y directions, respectively, defined as

$$E = \begin{Bmatrix} \rho U \\ \rho u U + p \\ \rho v U \\ (e+p)U + x_t p \end{Bmatrix}, \qquad F = \begin{Bmatrix} \rho V \\ \rho u V \\ \rho v V + p \\ (e+p)V + y_t p \end{Bmatrix} \tag{16}$$

The nomenclature adopted here is the usual one in CFD: ρ is the density, u and v are the Cartesian velocity components, and e is the total energy per unity of volume. The pressure, p, is given by the perfect gas equation, written as

$$p = (\gamma - 1)[e - \tfrac{1}{2}\rho(u^2 + v^2)] \tag{17}$$

Once again, as usual, γ represents the ratio of specific heats. The contravariant velocity components, U and V, are determined by

$$U = u - x_t \quad \text{and} \quad V = v - y_t \tag{18}$$

where x_t and y_t are the Cartesian components of the mesh velocity in the unsteady case.

B. Spatial Discretization

The adopted algorithm is based on a cell centered, finite volume scheme in which the stored information is actually the average value of the conserved properties throughout the entire control volume. These mean values are defined as

$$Q_i = \frac{1}{\Omega_i}\iint_{\Omega_i} Q \,\mathrm{d}x\,\mathrm{d}y \tag{19}$$

Equation (14) can then be rewritten for each ith cell as

$$\frac{\partial}{\partial t}(\Omega_i Q_i) + \int_{S_i} (E\,\mathrm{d}y - F\,\mathrm{d}x) = 0 \tag{20}$$

The remaining integration in Eq. (20) represents the flux of the E and F vector quantities through each control volume boundary. The code was developed to be used with unstructured meshes composed of triangles. The flux, therefore, can be evaluated as the sum of the flux contributions of each edge, which is obtained approximately from the average of the neighboring conserved quantities, as proposed by Jameson and Mavriplis [30]. Hence, the convective operator C is defined and it is given by

$$\int_{S_i} (E\,\mathrm{d}y - F\,\mathrm{d}x) \approx C_i = \sum_{k=1}^{3}[E_{ik}(y_{k_2} - y_{k_1}) - F_{ik}(x_{k_2} - x_{k_1})] \tag{21}$$

where the (x_{k_1}, y_{k_1}) and (x_{k_2}, y_{k_2}) coordinates are relative to the vertices that define the interface between the cells. The subscript ik designates the vector value at that interface. Such interface properties are evaluated using an average of the conserved variables, that is,

$$Q_{ik} = \tfrac{1}{2}(Q_i + Q_k) \tag{22}$$

It is also important to emphasize that, for the kth edge, the contravariant velocity components are given by

$$U_{ik} = u_{ik} - x_{t_k} \quad \text{and} \quad V_{ik} = v_{ik} - y_{t_k} \tag{23}$$

where u_{ik} and v_{ik} come from Q_{ik}, while x_{t_k} and y_{t_k} are the mean mesh velocity components of that edge, computed as the arithmetic average of the mesh velocity components of the two nodes that define the edge.

C. Artificial Dissipation

The Euler equations are a set of nondissipative hyperbolic conservation laws. Thus, as discussed by Pulliam [31], their numerical treatment requires an inherently dissipative discretization scheme or the introduction of artificial dissipation terms to avoid oscillations near shock waves and to damp high-frequency uncoupled error modes. Fletcher [32] demonstrates that, when the flux evaluation method adopted in the present CFD tool is applied in a regular mesh, it is analogous to a centered difference scheme in a finite difference formulation. In this case, Hirsch [33] shows that the addition of artificial dissipation terms is needed to avoid decoupling between the odd and even cell solutions due to high-frequency errors. Therefore, the spatially discrete Euler equations become

$$\frac{d}{dt}(\Omega_i Q_i) + C_i - D_i = 0 \tag{24}$$

where D represents the added artificial dissipation operator. Jameson et al. [34] state that an efficient way of constructing this dissipation operator is with a blend of second and fourth differences with coefficients that are proportional to local pressure gradients. Following such criterion, the dissipation operator implemented in the present CFD solver is analogous to the one presented by Batina [35], which is similar to the one given in [36]. However, the artificial dissipation operator used by Mavriplis [36] is appropriate for cell vertex schemes and, for this reason, some small modifications are performed to adapt such formulation for a cell centered code.

The fourth differences are responsible for the background dissipation that damps high-frequency errors, and they are given by a biharmonic operator. This operator is constructed by first forming an approximation to the Laplacian of the flow variables at each volume according to

$$\nabla^2 Q_i = \sum_{k=1}^{3}(Q_k - Q_i), \quad \text{or} \quad \nabla^2 Q_i = \sum_{k=1}^{3} Q_k - 3Q_i \tag{25}$$

where the sum is a result of the contribution from the three edges of the ith control volume. Mavriplis [36] suggests the use of the total enthalpy rather than the total energy in the last term of Q, to preserve a constant total enthalpy in the steady-state solution. Nevertheless, for simplicity's sake, this substitution is not implemented in the present solver. Results obtained over the years [22,24] show that the present approach does not significantly affect the final steady-state results. Finally, the biharmonic operator is given by

$$d^{(4)}(Q_i) = \sum_{k=1}^{3} \epsilon_{ik}^{(4)}(\nabla^2 Q_k - \nabla^2 Q_i)\left(\frac{A_k + A_i}{2}\right) \tag{26}$$

where $\epsilon_{ik}^{(4)}$ is a coefficient defined later, and

$$A_i = \sum_{k=1}^{3} |U_{ik}\Delta y_{ik} - V_{ik}\Delta x_{ik}| + a_{ik}\sqrt{(\Delta x_{ik})^2 + (\Delta y_{ik})^2} \tag{27}$$

The summation present in Eq. (27) is performed over all edges of the ith control volume. The subscript ik denotes the edge properties given by the average of the properties of the neighboring volumes as in Eq. (22). This construction of A_i represents the maximum eigenvalue of the Euler equations $|U| + a$ in the direction normal to each control volume boundary edge, integrated around the boundary of the ith control volume. Mavriplis [36] states that this approach is consistent with the finite volume formulation and also provides an isotropic value for scaling the dissipation with the maximum local eigenvalue. Furthermore, the averaging of the A_i and A_k terms assures that the contribution of the dissipation operator on each edge will be equivalent but opposite for neighboring control volumes. Thus, this approach guarantees that the added dissipation is conservative. Moreover, according to Jameson and Mavriplis [30], the Laplacian term given by Eq. (25) is of order $(\Delta x)^2$. Therefore, the biharmonic operator is of order $(\Delta x)^3$, and the accuracy of the scheme is preserved.

However, this biharmonic operator is not able to damp oscillations that appear in regions of high gradients, such as those in the vicinity of shock waves. For this reason, many artificial dissipation formulations proposed in the literature, for example [30,34–36], also include second difference terms that offer higher levels of dissipation where needed. Mavriplis [36] suggests the use of a Laplacian operator as a means of providing the second differences. Such operator is given by

$$d^{(2)}(Q_i) = \sum_{k=1}^{3} \epsilon_{ik}^{(2)}(Q_k - Q_i)\left(\frac{A_k + A_i}{2}\right) \tag{28}$$

To ensure that this Laplacian operator is significant only in the desired regions, the coefficient $\epsilon_{ik}^{(2)}$ is proportional to an undivided Laplacian in the pressure given by

$$\nu_i = \frac{\sum_{k=1}^{3} |p_k - p_i|}{\sum_{k=1}^{3}(p_k + p_i)} \tag{29}$$

The Laplacian operator should also be conservative. The approach adopted by Mavriplis [36] fails to do so and, therefore, a slightly different formulation is implemented in the present work, based on the ideas of [30]. Instead of using a different value of ν for each control volume, which leads to a nonconservative operator, $\epsilon_{ik}^{(2)}$ is proportional to ν_{ik}, defined as

$$\nu_{ik} = \max(\nu_i, \nu_k) \tag{30}$$

Finally, $\epsilon_{ik}^{(2)}$ is given by

$$\epsilon_{ik}^{(2)} = K^{(2)}\nu_{ik} \tag{31}$$

where $K^{(2)}$ is a user defined constant, which is determined empirically. As a consequence of this construction, the Laplacian operator is of order (Δx). The coefficient $\epsilon_{ik}^{(4)}$ cited in Eq. (26) is used to trigger the fourth differences on and off, according to the smoothness of the flow. It is defined as

$$\epsilon_{ik}^{(4)} = \max(0, K^{(4)} - \epsilon_{ik}^{(2)}) \tag{32}$$

where $K^{(4)}$ is also a constant the user can choose arbitrarily. The values adopted for these user defined constants are [13,34,36]

$$K^{(2)} = \tfrac{1}{2} \quad \text{and} \quad K^{(4)} = \tfrac{3}{256} \tag{33}$$

They have been widely tested and proved to produce good results [17,22]. Finally, the artificial dissipation operator is given by

$$D_i = d_i^{(2)} - d_i^{(4)} \tag{34}$$

D. Time Discretization

The numerical solution is advanced in time using a second-order accurate, five-stage, explicit hybrid scheme, which evolved from the consideration of Runge–Kutta time stepping schemes [30,36]. This scheme, already including the necessary terms to account for changes in cell area due to mesh motion or deformation [35], can be written as

$$\begin{aligned}
Q_i^{(0)} &= Q_i^n, \qquad Q_i^{(1)} = \frac{\Omega_i^n}{\Omega_i^{n+1}} Q_i^{(0)} - \Theta_1 \frac{\Delta t_i}{\Omega_i^{n+1}}\left[C_i^{(0)} - D_i^{(0)}\right],\\
Q_i^{(2)} &= \frac{\Omega_i^n}{\Omega_i^{n+1}} Q_i^{(0)} - \Theta_2 \frac{\Delta t_i}{\Omega_i^{n+1}}\left[C_i^{(1)} - D_i^{(1)}\right],\\
Q_i^{(3)} &= \frac{\Omega_i^n}{\Omega_i^{n+1}} Q_i^{(0)} - \Theta_3 \frac{\Delta t_i}{\Omega_i^{n+1}}\left[C_i^{(2)} - D_i^{(1)}\right],\\
Q_i^{(4)} &= \frac{\Omega_i^n}{\Omega_i^{n+1}} Q_i^{(0)} - \Theta_4 \frac{\Delta t_i}{\Omega_i^{n+1}}\left[C_i^{(3)} - D_i^{(1)}\right],\\
Q_i^{(5)} &= \frac{\Omega_i^n}{\Omega_i^{n+1}} Q_i^{(0)} - \Theta_5 \frac{\Delta t_i}{\Omega_i^{n+1}}\left[C_i^{(4)} - D_i^{(1)}\right], \qquad Q_i^{n+1} = Q_i^{(5)}
\end{aligned} \tag{35}$$

where the superscripts n and $(n+1)$ indicate that these are property values at the beginning and the end of the nth time step, respectively. The values used for the Θ coefficients, as suggested by Mavriplis [36], are

$$\Theta_1 = \tfrac{1}{4}, \qquad \Theta_2 = \tfrac{1}{6}, \qquad \Theta_3 = \tfrac{3}{8}, \qquad \Theta_4 = \tfrac{1}{2}, \qquad \Theta_5 = 1 \quad (36)$$

In Eq. (35), the convective operator C is evaluated at every stage of the integration process, but the artificial dissipation operator D is only evaluated at the two initial stages. This is done with the objective of saving computational time because the evaluation of the latter is rather expensive. As discussed by Jameson et al. [34], this type of procedure is known to provide adequate numerical damping characteristics while achieving the desired reduction in computational cost.

Steady-state solutions for the mean flight condition of interest must be obtained before the unsteady calculation can be started. Therefore, it is also important to guarantee an acceptable efficiency for the code in steady-state mode. In the present work, both local time stepping and implicit residual smoothing [30,37,38] are employed to accelerate convergence to steady state. More details on convergence acceleration techniques are found in [13,24].

E. Boundary Conditions

Although the CFD solver in question is prepared for a large number of flow situations, for the cases treated in the present work, only two boundary conditions are relevant: wall and far field. Furthermore, the boundary condition implementation follows the concept of ghost volumes. This means that nonphysical volumes are imposed as neighbors to the real boundary volumes in a fashion that the flux vectors evaluated at the interface end up taking the desired conditions into consideration.

For Euler flows, the wall condition is that the flow must be tangent to the surface. This is accomplished by setting the normal component of the contravariant velocity equal to zero at the wall, whereas the tangential velocity remains unaltered. Therefore, according to the flux calculation algorithm just presented, the normal component of the contravariant velocity at the wall is given by

$$U_{n_w} = \tfrac{1}{2}[s_y(u_i + u_g - 2x_{t_{ig}}) - s_x(v_i + v_g - 2y_{t_{ig}})] = 0 \quad (37)$$

where

$$s_x = \frac{x_{ig_2} - x_{ig_1}}{\sqrt{(x_{ig_2} - x_{ig_1})^2 + (y_{ig_2} - y_{ig_1})^2}} \quad (38)$$

$$s_y = \frac{y_{ig_2} - y_{ig_1}}{\sqrt{(x_{ig_2} - x_{ig_1})^2 + (y_{ig_2} - y_{ig_1})^2}} \quad (39)$$

and the subscript ig designates the interface between the ith volume and the corresponding ghost volume. Furthermore, the tangential velocity component in the ghost volume is given by

$$u_{t_g} = s_x u_g + s_y v_g = s_x u_i + s_y v_i = u_{t_i} \quad (40)$$

Therefore, from Eqs. (37) and (40), the ghost volume velocity components are

$$u_g = 2s_x s_y(v_i - y_{t_{ig}}) + (s_x^2 - s_y^2)(u_i - x_{t_{ig}}) + x_{t_{ig}} \quad (41)$$

$$v_g = 2s_x s_y(u_i - x_{t_{ig}}) + (s_y^2 - s_x^2)(v_i - y_{t_{ig}}) + y_{t_{ig}} \quad (42)$$

The other two flow variables result from the assumptions of zero normal temperature and pressure gradients at the wall. The zero normal temperature gradient assumption works as an extrapolation of the interior flow properties, which gives the correct physical behavior for temperature at the wall. This procedure implies a zero normal internal energy gradient. Furthermore, the tangential flow conditions just presented also yield a zero normal kinetic energy gradient. Therefore, the temperature condition ultimately results in a zero normal total energy gradient at the wall. The pressure condition is an approximation, which holds exactly only for a flat plate. The real boundary condition for the pressure gradient should take into consideration the body curvature [33]. It is believed that this approximation has led to some small fluctuations in the pressure distribution results along the wall, [‡] but it does not compromise the solution as a whole. Hence, one can write

$$e_g = e_i, \quad \text{and} \quad p_g = p_i \quad (43)$$

which, when combined, also result in

$$\rho_g = \rho_i \quad (44)$$

The far-field boundary is treated as a nonreflexive one in order to allow for the propagation of the waves leaving and entering the finite computational domain. In the present work, this is done considering the Riemann invariants for a locally one-dimensional subsonic flow, which are defined as

$$R^- = U_{n_f} - \frac{2a_f}{\gamma - 1} \quad (45)$$

$$R^+ = U_{n_f} + \frac{2a_f}{\gamma - 1} \quad (46)$$

where U_{n_f} is the contravariant velocity component normal to the boundary, and a_f is the local sound speed. As the invariant R^- is constant along a characteristic wave that propagates inwards with respect to the computational domain, it can be determined from the undisturbed flow conditions. In an analogous way, R^+ is constant along a characteristic wave which propagates outwards, and, hence, it can be approximated with the interior volume properties. Thus,

$$R_\infty^- = u_{n_\infty} - x_{t_{nf}} - \frac{2a_\infty}{\gamma - 1} \quad (47)$$

$$R_i^+ = u_{n_i} - x_{t_{nf}} + \frac{2a_i}{\gamma - 1} \quad (48)$$

where

$$u_{n_\infty} = U_\infty[s_y \cos(\alpha_\infty) - s_x \sin(\alpha_\infty)] \quad (49)$$

$$u_{n_i} = s_y u_i - s_x v_i \quad (50)$$

and

$$x_{t_{nf}} = s_y x_{t_f} - s_x y_{t_f} \quad (51)$$

In the preceding equations, α_∞ represents the undisturbed flow angle of attack. From Eqs. (45–48), it follows that the interface properties U_{n_f} and a_f can be written as

$$U_{n_f} = \frac{1}{2}(R_i^+ + R_\infty^-) \quad (52)$$

$$a_f = \frac{\gamma - 1}{4}(R_i^+ - R_\infty^-) \quad (53)$$

Once the value of U_{n_f} is known, it is possible to determine whether the other characteristics are entering or leaving the domain. Therefore, there are two possibilities:

1) Exit boundary ($U_{n_f} > 0$): entropy and tangential velocity component are extrapolated from interior volume using isentropic relations

$$\rho_f = \left(\frac{\rho_i^\gamma a_f^2}{p_i \gamma}\right)^{\frac{1}{1-\gamma}} \quad (54)$$

[‡]Simões, C. F. C., private communication, May 2006.

$$u_f = u_i + s_y(U_{n_f} - u_{n_i} + x_{t_{nf}}) \tag{55}$$

$$v_f = v_i - s_x(U_{n_f} - u_{n_i} + x_{t_{nf}}) \tag{56}$$

$$p_f = \frac{\rho_f a_f^2}{\gamma} \tag{57}$$

$$e_f = \frac{p_f}{\gamma - 1} + \frac{1}{2}\rho_f(u_f^2 + v_f^2) \tag{58}$$

2) Entrance boundary ($U_{n_f} < 0$): entropy and tangential velocity component are extrapolated from undisturbed flow conditions using isentropic relations

$$\rho_f = \left(\frac{\rho_\infty^\gamma a_f^2}{p_\infty \gamma}\right)^{\frac{1}{1-\gamma}} \tag{59}$$

$$u_f = U_\infty \cos(\alpha_\infty) + s_y(U_{n_f} - u_{n_\infty} + x_{t_{nf}}) \tag{60}$$

$$v_f = U_\infty \sin(\alpha_\infty) - s_x(U_{n_f} - u_{n_\infty} + x_{t_{nf}}) \tag{61}$$

$$p_f = \frac{\rho_f a_f^2}{\gamma} \tag{62}$$

$$e_f = \frac{p_f}{\gamma - 1} + \frac{1}{2}\rho_f(u_f^2 + v_f^2) \tag{63}$$

The properties at the boundary are calculated as the average between the interior and ghost volumes, and, therefore,

$$Q_g = 2Q_f - Q_i \tag{64}$$

It is important to emphasize that such formulation is only valid for noncirculatory flows. Hence, there is an intrinsic error associated with this nonreflexive boundary implementation. But this error is diminished by making the far-field boundary sufficiently distant from the aerodynamic body.

F. Mesh Generation and Movement

The meshes used in the present work are generated with the commercial grid generator ICEM CFD©. Figure 3 shows two views of the mesh around a NACA 0012 airfoil, which is employed to obtain the results discussed here.

Unsteady calculations involve body motion and, therefore, the computational mesh should be somehow adjusted to take this motion into account. Two approaches are adopted in the present work. The first one follows the ideas presented in [35], according to which the sides of the triangles that constitute the mesh are modeled as springs with stiffness constants inversely proportional to their lengths. Hence, for each edge between j and ℓ nodes, the stiffness constant is defined as

$$\mathcal{K}_{(j,\ell)} = \frac{1}{[(x_\ell - x_j)^2 + (y_\ell - y_j)^2]^{\frac{\mathcal{P}}{2}}} \tag{65}$$

where $\mathcal{P}$ is a user-defined parameter. Furthermore, the far-field boundary is kept fixed, whereas the body nodes are moved according to a predefined pattern. Hence, the interior node positions can be determined from a linear system constructed for the static equilibrium of the springs. An iterative predictor–corrector method is employed for the solution of such system, namely,

$$\tilde{\delta}x_j = 2\delta x_j^n - \delta x_j^{n-1} \tag{66}$$

$$\tilde{\delta}y_j = 2\delta y_j^n - \delta y_j^{n-1} \tag{67}$$

$$\delta x_j^{n+1} = \frac{\sum_\ell \mathcal{K}_{(j,\ell)}\tilde{\delta}x_\ell}{\sum_\ell \mathcal{K}_{(j,\ell)}} \tag{68}$$

$$\delta y_j^{n+1} = \frac{\sum_\ell \mathcal{K}_{(j,\ell)}\tilde{\delta}y_\ell}{\sum_\ell \mathcal{K}_{(j,\ell)}} \tag{69}$$

The new position of the interior nodes are, then, given by

$$x_j^{n+1} = x_j^n + \delta x_j^{n+1} \tag{70}$$

$$y_j^{n+1} = y_j^n + \delta y_j^{n+1} \tag{71}$$

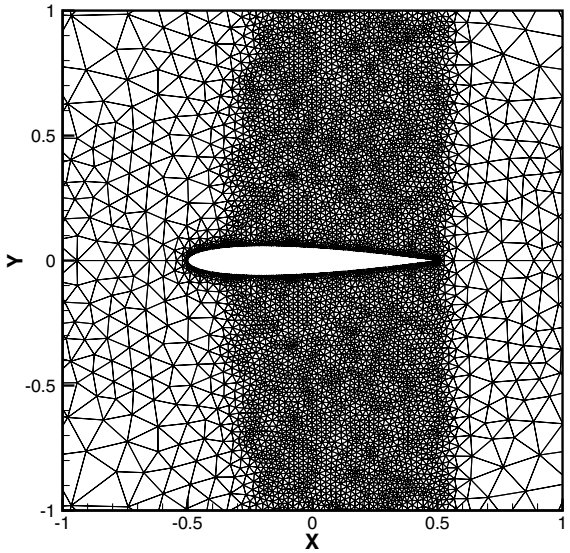

a) Mesh view around the NACA 0012 airfoil

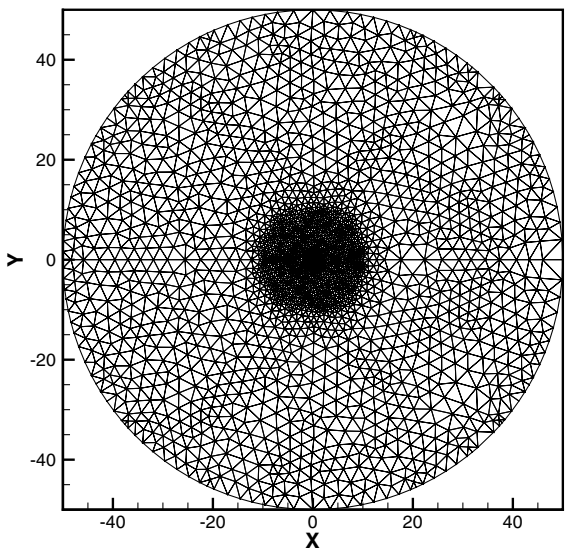

b) Complete mesh, with 8323 nodes and 16,232 volumes

Fig. 3 Mesh around NACA 0012 profile with 292 wall points and 50 chord lengths of distance between the body and the far field.

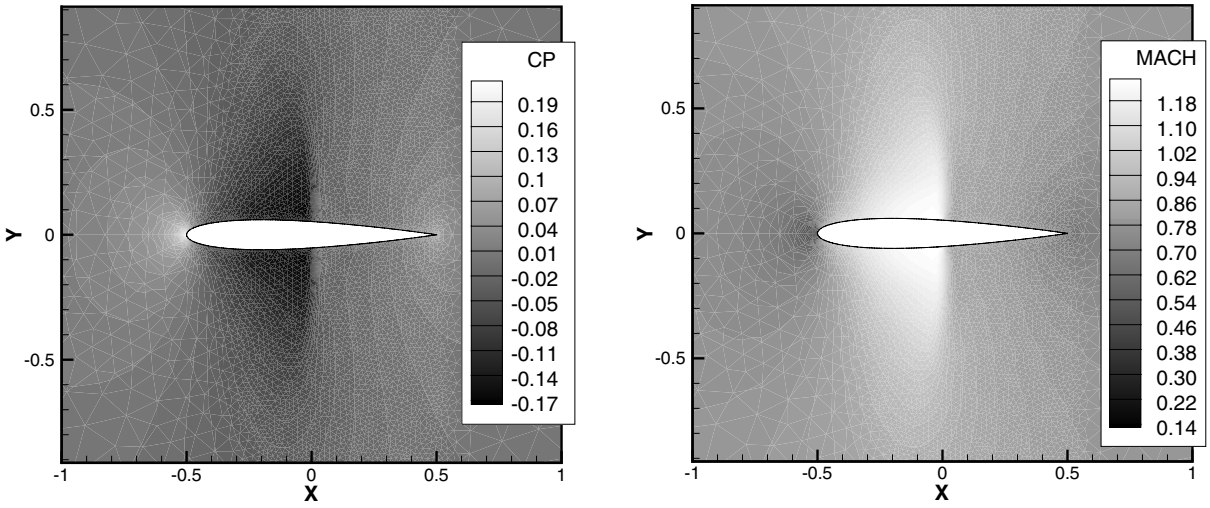

a) Pressure coefficient contours **b) Mach number contours**

Fig. 4 Steady state solution for a NACA 0012 airfoil at $M_\infty = 0.8$ and $\alpha_0 = 0$.

It is observed that the mesh quality is directly dependent on the value of the parameter $\mathcal{P}$ and on the number of Jacobi iterations used in the solution process. The present authors use $\mathcal{P} = 1$ and five iterations in all cases, and these values have shown to present satisfactory results.

The other way of accounting for the motion of the body is to rigidly move the mesh accordingly. It is important to notice that, in this approach, the far-field boundary is no longer kept fixed, but it moves together with the rest of the mesh. The far-field boundary conditions presented in the last section already account for this motion. Of course this approach is less computationally expensive than the preceding one, but it is not as general because it can only be used when the structural modes involve rigid body motions. Furthermore, the second approach is also used in the current calculations to demonstrate the influence of the mesh deformation in the solutions, as it is shown later.

Moreover, independent of the method used, the mesh velocity components can be approximated by

$$x_{t_j} = \frac{x_j^{n+1} - x_j^n}{\Delta t} \tag{72}$$

$$y_{t_j} = \frac{y_j^{n+1} - y_j^n}{\Delta t} \tag{73}$$

The new cell areas are determined employing the geometric conservation law concept [39], in which the total area conservation is imposed in a similar manner to the other flow conserved variables.

V. Results and Discussion

A. General Considerations

Before attempting applications of the proposed analyses, some validation simulations are performed with the CFD tool. This has been done throughout the entire development of this code, as can be seen in [13,17,22,24,40]. Once the CFD tool is tested and proves to be reliable, the next step is to proceed in obtaining the unsteady responses of interest. The test case considered throughout this paper involves a NACA 0012 airfoil at $M_\infty = 0.8$, that is, in transonic regime, and $\alpha_0 = 0$. The pressure coefficient and Mach number contours of the steady-state solution are shown in Fig. 4. As one can see, the present results are capable of representing the physical phenomena expected for the flows of interest, including the strong shock waves that occur over the airfoil. Furthermore, Fig. 5 presents the pressure coefficient distribution over the airfoil surface, and comparisons with the numerical results available in [41] (Lit. Num.) and experimental results found in [42] (Lit. Exp.). As mentioned before, the present results show a small oscillation in the pressure coefficient distribution, and it is believed that this occurs due to approximations in the wall boundary conditions, but these oscillations do not affect the overall adequacy of the solution. This is rather confirmed by the good agreement between the present solution and that of [41]. Moreover, although one cannot expect that Euler results exactly match experimental measurements, Fig. 5 shows that, except for the vicinity of shock waves, where viscous effects are bound to increase due to shock–boundary layer interaction, the numerical pressure coefficient distribution is very close to the experimental one.

Rausch et al. [43] present frequency domain responses for the transonic configuration in question when the airfoil is submitted to both plunging and pitching motions. These responses are obtained numerically with a solver very similar to the one used in the present work. Furthermore, [43] also applies the pulse transfer function technique, that is, the solutions are obtained with a smooth input, and, therefore, it serves as a good standard for comparison. The present authors attempt to reproduce these solutions using exponentially shaped, unit sample, discrete step, and harmonic inputs to address the capabilities of obtaining impulsive and indicial aerodynamic responses with modern CFD solvers. Moreover, this is done with both deformable and rigid mesh formulations. It is important to emphasize that the pitching motion occurs over the quarter-chord point of the airfoil. Additionally, C_ℓ and C_m denote the lift and moment coefficients, respectively. Moreover, the values presented here for these coefficients are actually the differences in relation to the steady-state values. For a NACA 0012 airfoil with $\alpha_0 = 0$, one

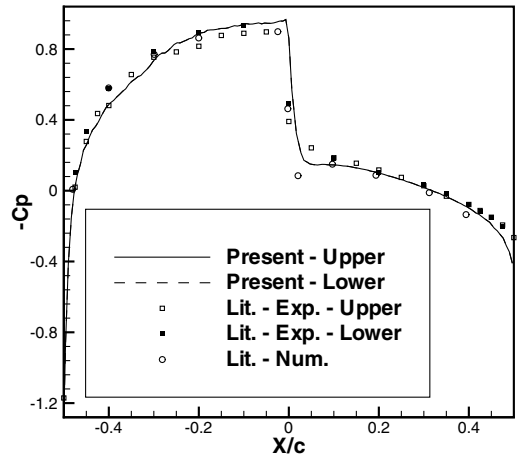

Fig. 5 Steady-state pressure coefficient distribution over a NACA 0012 airfoil at $M_\infty = 0.8$ and $\alpha_0 = 0$. "Upper" and "Lower" represent the respective airfoil surface.

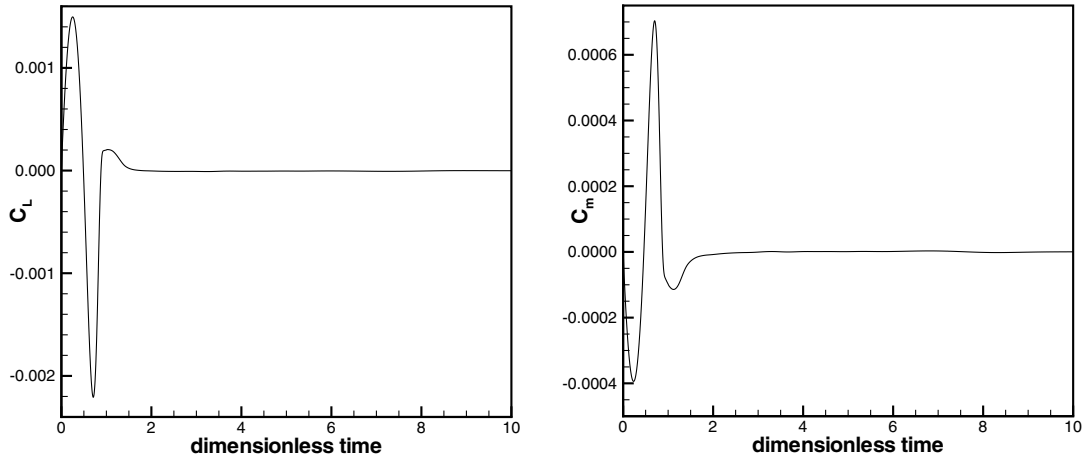

a) C_l time history b) C_m time history

Fig. 6 Initial part of the response of a NACA 0012 airfoil at $M_\infty = 0.8$ and $\alpha_0 = 0$ to an EP in plunge.

would expect zero lift and moment, but numerical errors lead to small residual values. Finally, henceforth, the pitching moment refers to the quarter-chord point and is positive in the nose-up direction.

B. Deformable Mesh

Figure 6 shows the time history of the solution in terms of the aerodynamic coefficients C_ℓ and C_m for an exponentially shaped pulse (EP) input in plunge. This input extends until the dimensionless time value of 1 and it has maximum value of $0.0001c$. The total integration time is 300 dimensionless time units, but only the initial part of the solution is shown to emphasize the most relevant transient response. Moreover, the time step used for all cases presented here is 0.003 dimensionless time units, which is the largest value possible considering numerical stability limit of the time-marching scheme employed. The same sort of solution is obtained for a pitching motion with a similar input of amplitude 0.001 deg. The corresponding time responses are given in Fig. 7.

The simulation of the unit sample (US) and discrete step (DS) excitations is also attempted. Figures 8 and 9 show the time responses to unit sample inputs of amplitudes $0.000001c$ in plunge and 0.0001 deg in pitch, respectively. In an analogous way, Figs. 10 and 11 present the time responses to discrete step inputs of amplitudes $0.000001c$ in plunge and 0.0001 deg in pitch. For these last cases, the solution is only shown up to the dimensionless time value of 0.1, because the transient part dies out much more quickly, as expected. For the discrete step pitching motion, the solutions in terms of the aerodynamic coefficients tend to asymptotic values different from zero because the final position of the airfoil is not the same as the initial one.

The frequency domain impulsive responses obtained from these time solutions are presented in Figs. 12 and 13, together with values resultant from harmonic (H) oscillation simulations and the literature data of [43] (Lit.). It can be seen that the exponentially shaped responses match the harmonic ones in both modes, which is a proof of the validity of the adopted hypothesis of linearity in relation to the motion amplitude, and that the EP input can adequately excite the frequency range of interest. Moreover, these results also agree very well with the literature data, what corroborates the quality of the present CFD solver. Nevertheless, the responses obtained directly with discrete step and unit sample inputs deviate from the expected values. Specifically, the plunge mode results for these inputs present nonzero values for a steady-state response, which makes no physical sense at all. However, the results are not completely different from the EP responses, which might indicate numerical difficulties rather than inadequacies in the solution procedure.

It is very important to recall the discussion of Sec. III about the correct definition of the aerodynamic input function. According to the argument of [14], it is not possible to determine impulsive frequency domain aerodynamic responses in the plunge mode performing the division of the DFT of the CFD response by the DFT of a smooth excitation due to a two-channel input dependency of the aerodynamic input function. However, the perfect agreement between the impulsive frequency domain responses obtained with the EP and the values acquired with the harmonic oscillations in the plunge mode proves that the single-input premise is valid, as explained in Sec. III.

To understand the behavior reported in Figs. 12 and 13, it is important to analyze the effect of the mesh deformation on the

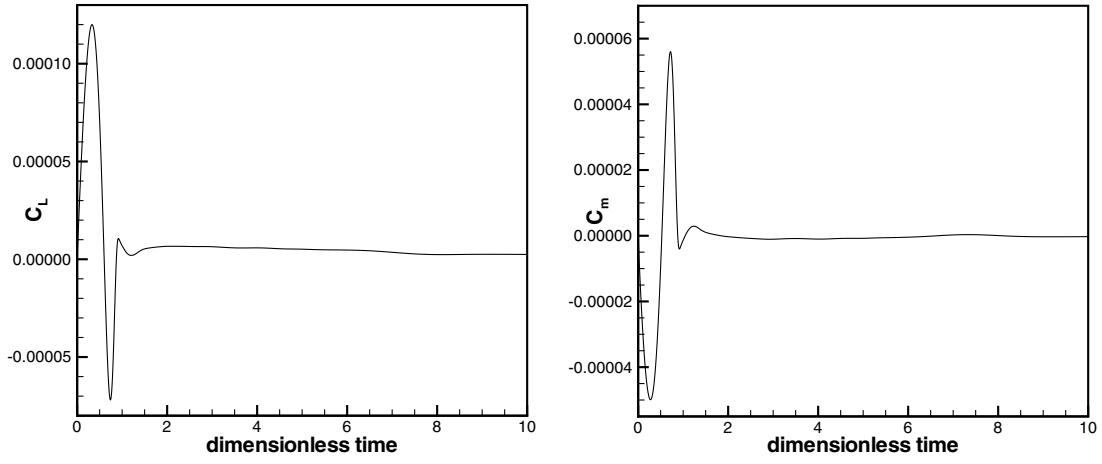

a) C_l time history b) C_m time history

Fig. 7 Initial part of the response of a NACA 0012 airfoil at $M_\infty = 0.8$ and $\alpha_0 = 0$ to an EP in pitch.

aerodynamic solutions. The present mesh deformation algorithm is constructed in a way that the elements far from the body should absorb most of the motion, whereas the grid around it remains practically unchanged. This is done to avoid, or attenuate, spurious fluctuations that might occur in the solution due to the grid dependency of the numerical scheme because the mesh near the body is more important in solving the major phenomena that dominate the aerodynamic response. The fact is that this procedure works well for smooth motions, such as the exponentially shaped pulse, but it is not effective for sharp inputs. This reasoning is reinforced by analyzing

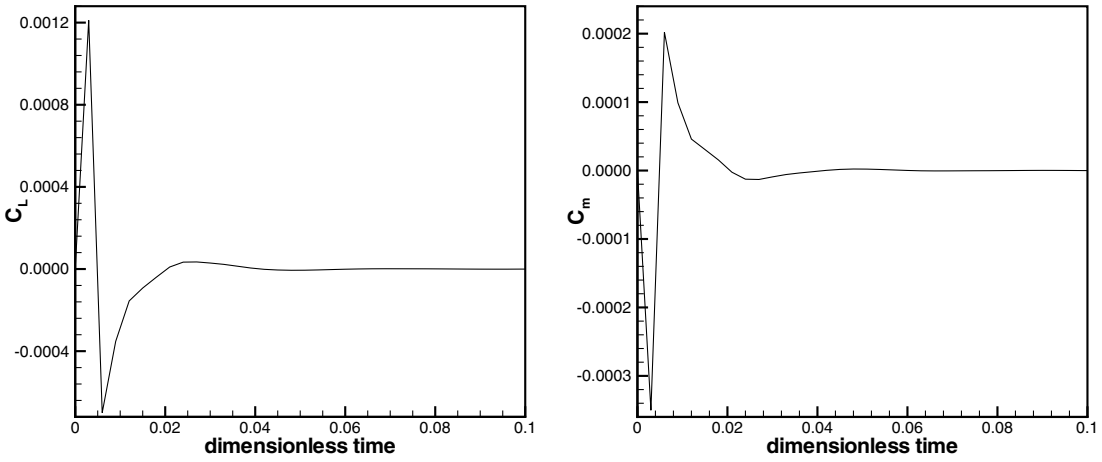

a) C_l time history b) C_m time history

Fig. 8 Initial part of the response of a NACA 0012 airfoil at $M_\infty = 0.8$ and $\alpha_0 = 0$ to a US in plunge.

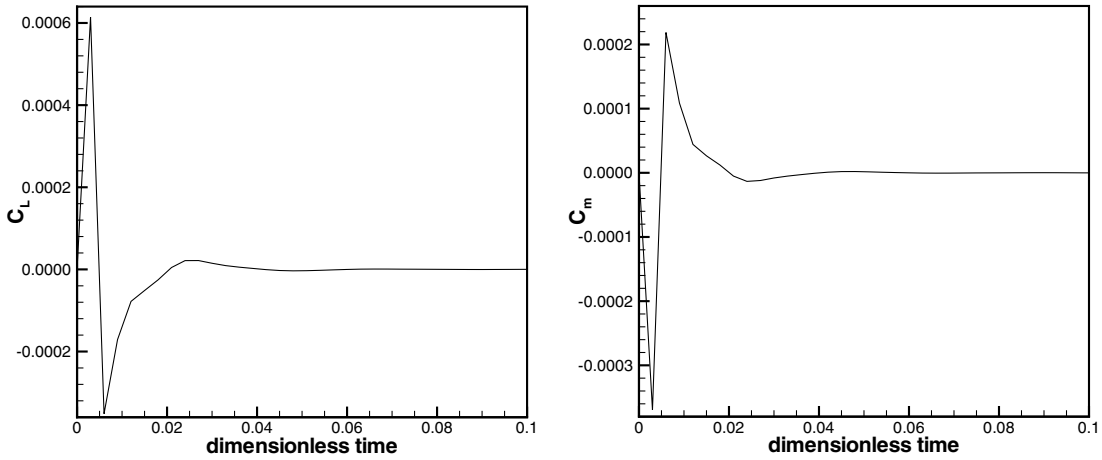

a) C_l time history b) C_m time history

Fig. 9 Initial part of the response of a NACA 0012 airfoil at $M_\infty = 0.8$ and $\alpha_0 = 0$ to a US in pitch.

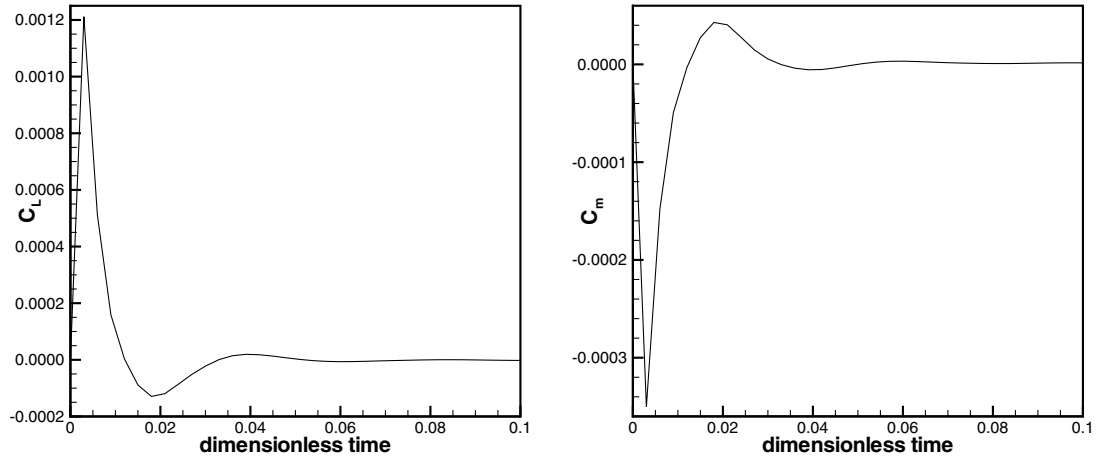

a) C_l time history b) C_m time history

Fig. 10 Initial part of the response of a NACA 0012 airfoil at $M_\infty = 0.8$ and $\alpha_0 = 0$ to a DS in plunge.

the response for the same exponentially shaped pulse, but keeping the mesh without any deformation, except for the wall, presented in Figs. 14 and 15. Of course, this is only possible when the input amplitude is small enough such that the wall does not cross the neighboring volumes. In this case, the EP gives the same results as the DS excitation with mesh deformation, in both modes. The agreement with the US solution is not excellent for the plunging motion, but it is much better than in the prior situation. On the other

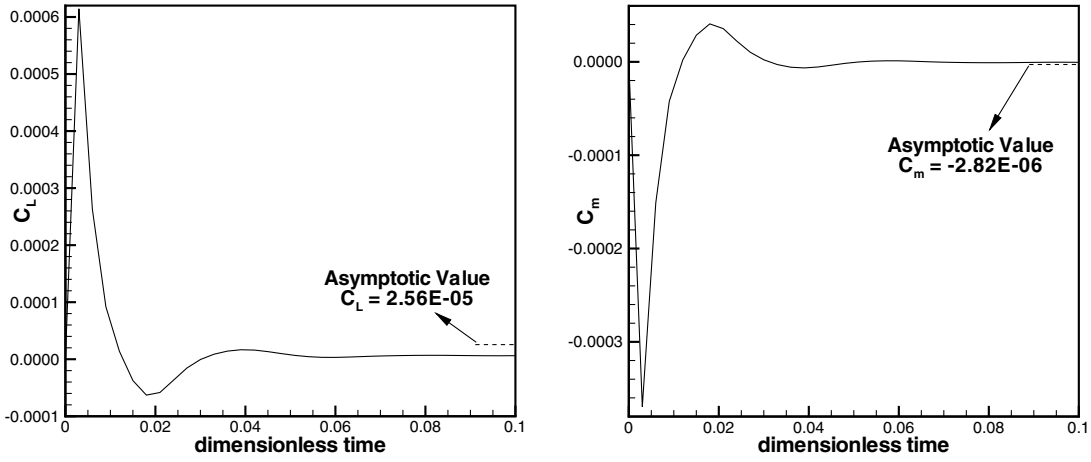

a) C_l time history b) C_m time history

Fig. 11 Initial part of the response of a NACA 0012 airfoil at $M_\infty = 0.8$ and $\alpha_0 = 0$ to a DS in pitch.

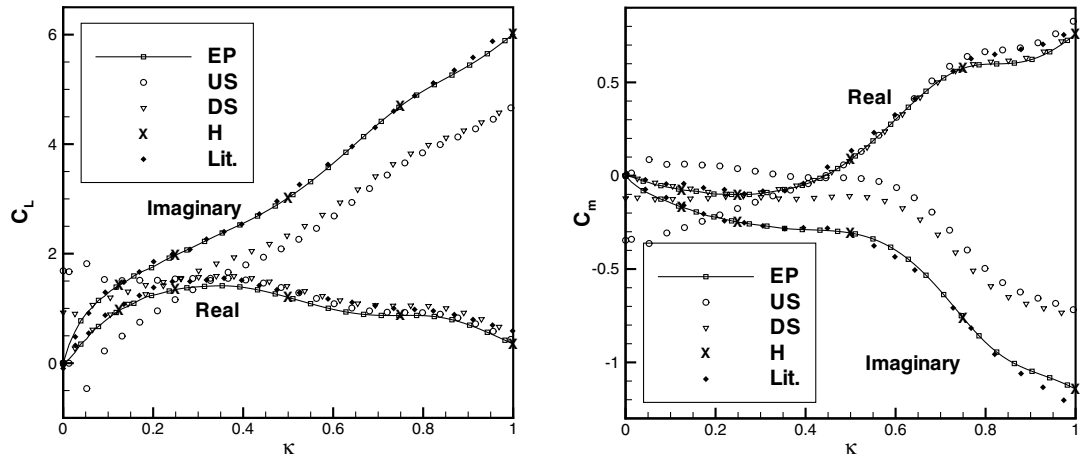

a) C_l frequency domain response b) C_m frequency domain response

Fig. 12 Low reduced frequency impulsive responses of a NACA 0012 airfoil at $M_\infty = 0.8$ and $\alpha_0 = 0$ to inputs in plunge.

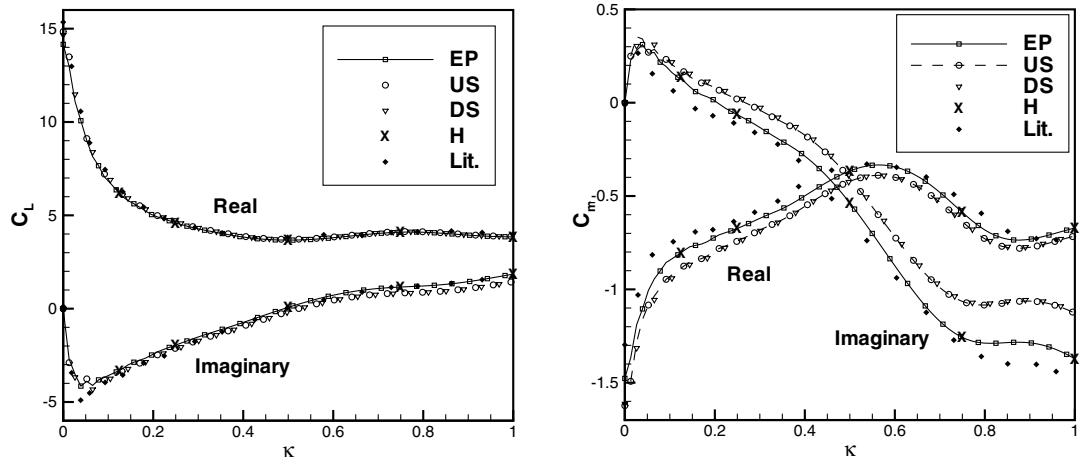

a) C_l frequency domain response b) C_m frequency domain response

Fig. 13 Low reduced frequency impulsive responses of a NACA 0012 airfoil at $M_\infty = 0.8$ and $\alpha_0 = 0$ to inputs in pitch.

hand, for the pitching motion, the EP solution, considering only the wall motion, and the US solution, with mesh deformation, show an excellent matching. This indicates that, for the US and DS inputs, the dynamic mesh algorithm is not effective in avoiding the mesh deformation around the body, which causes numerical errors.

C. Rigid Mesh

The mesh deformation effects observed in the results presented in the preceding section drove the authors to explore the possibility of rigidly moving the mesh, following the body motion, and, consequently, without volume deformations. Naturally, this can only

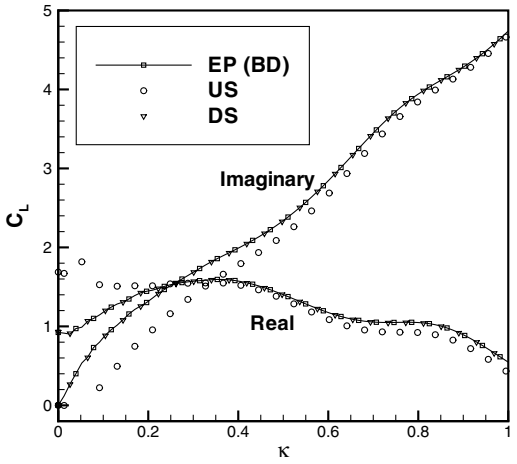

a) C_l frequency domain response

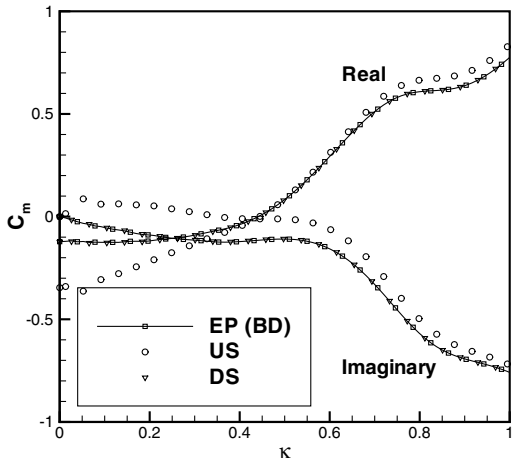

b) C_m frequency domain response

Fig. 14 Low reduced frequency impulsive responses of a NACA 0012 airfoil at $M_\infty = 0.8$ and $\alpha_0 = 0$ to inputs in plunge. BD indicates that only the body nodes move, without mesh deformation.

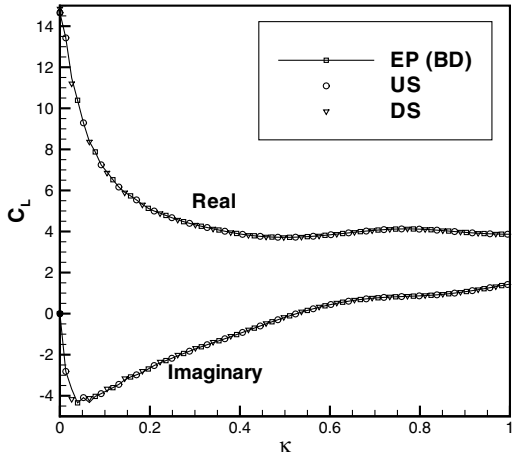

a) C_l frequency domain response

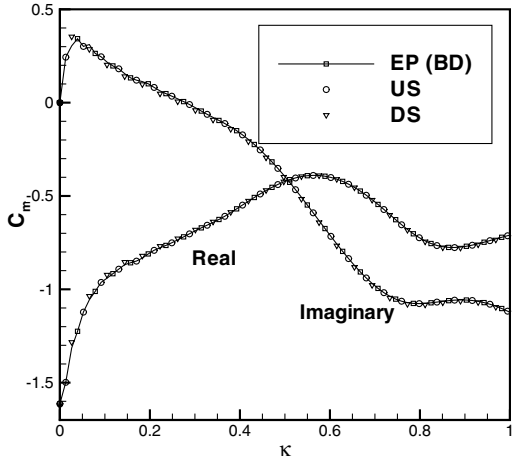

b) C_m frequency domain response

Fig. 15 Low reduced frequency impulsive responses of a NACA 0012 airfoil at $M_\infty = 0.8$ and $\alpha_0 = 0$ to inputs in pitch. BD indicates that only the body nodes move, without mesh deformation.

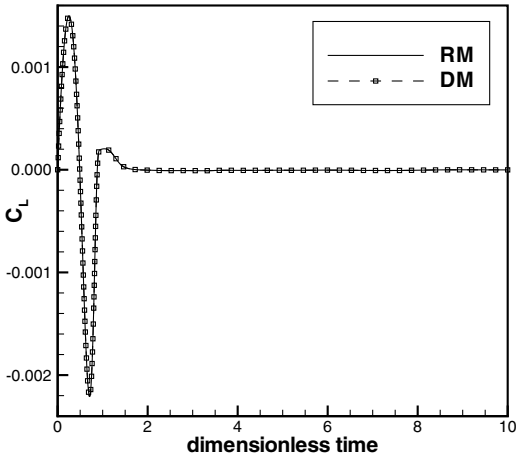

a) C_l time history

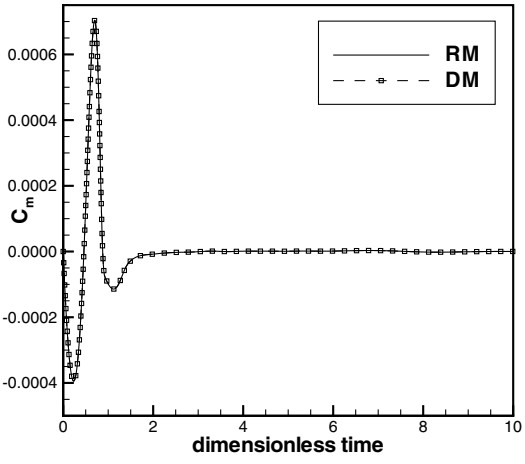

b) C_m time history

Fig. 16 Initial part of the response of a NACA 0012 airfoil at $M_\infty = 0.8$ and $\alpha_0 = 0$ to an EP in plunge. Comparison between deformable (DM) and rigid mesh (RM) simulations.

be done in the cases in question because the body exclusively performs rigid motions. This type of simulation is not possible for the modal analysis of deformable structures. The simulations performed with the rigid mesh algorithm are exactly the same ones analyzed before. Hence, once again, the NACA 0012 airfoil is submitted to exponentially shaped pulse, unit sample, discrete step, and harmonic inputs, in both pitch and plunge modes. The excitation amplitudes are also the same as the ones previously presented. The time responses for such simulations, except harmonic oscillations, are given in Figs. 16–21, together with the corresponding deformable

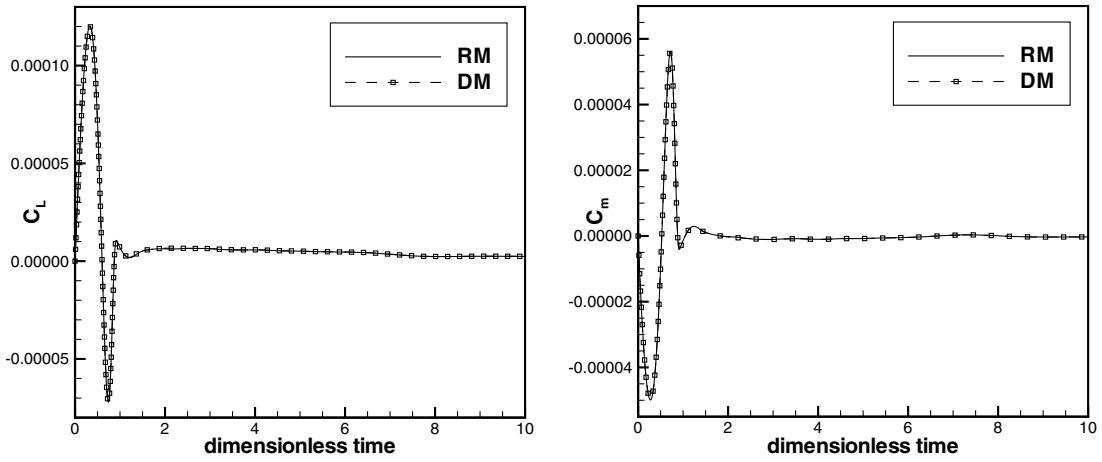

a) C_l time history b) C_m time history

Fig. 17 Initial part of the response of a NACA 0012 airfoil at $M_\infty = 0.8$ and $\alpha_0 = 0$ to an EP in pitch. Comparison between DM and RM simulations.

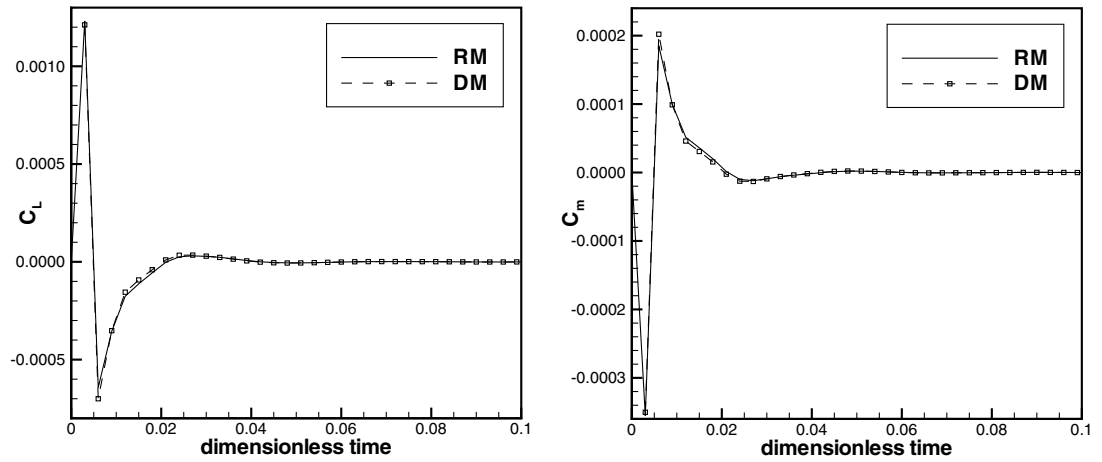

a) C_l time history b) C_m time history

Fig. 18 Initial part of the response of a NACA 0012 airfoil at $M_\infty = 0.8$ and $\alpha_0 = 0$ to a US in plunge. Comparison between DM and RM simulations.

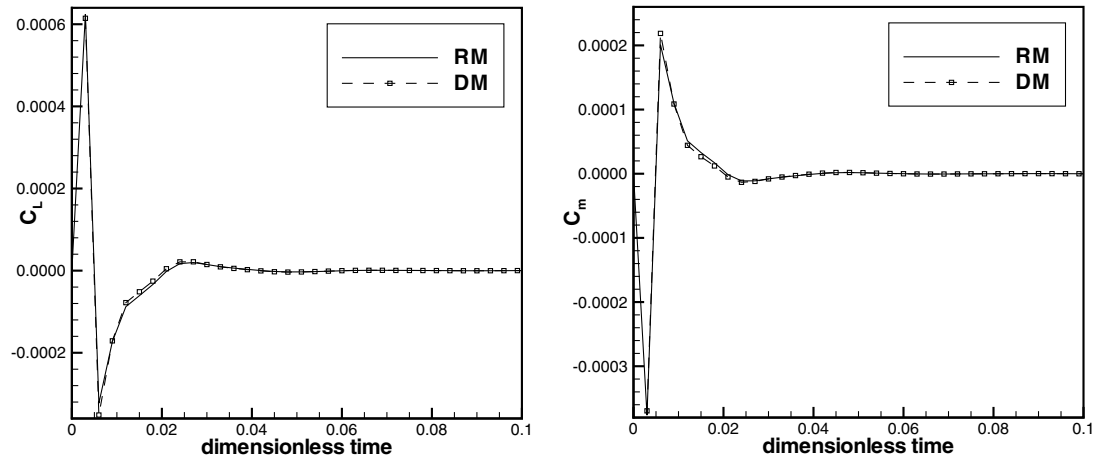

a) C_l time history b) C_m time history

Fig. 19 Initial part of the response of a NACA 0012 airfoil at $M_\infty = 0.8$ and $\alpha_0 = 0$ to a US in pitch. Comparison between DM and RM simulations.

mesh results. In the case of a discrete step pitch motion, the asymptotic value indicated corresponds to the rigid mesh (RM) solution because the deformable mesh (DM) value is given in Fig. 11.

The agreement between RM and DM time domain solutions for the EP cases is quite evident. However, when US and DS responses are considered, there are small differences. It is very hard to say from the time solutions alone whether these differences exert considerable impact on the overall solution. This question is answered with the analysis of the frequency domain impulsive responses for the cases with a rigid mesh, given in Figs. 22 and 23. These figures show that

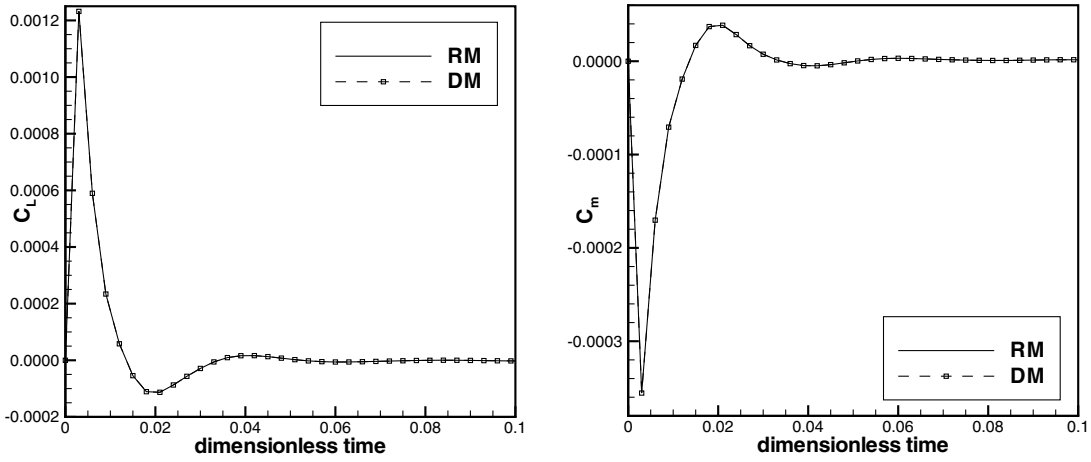

a) C_l time history b) C_m time history

Fig. 20 Initial part of the response of a NACA 0012 airfoil at $M_\infty = 0.8$ and $\alpha_0 = 0$ to a DS in plunge. Comparison between DM and RM simulations.

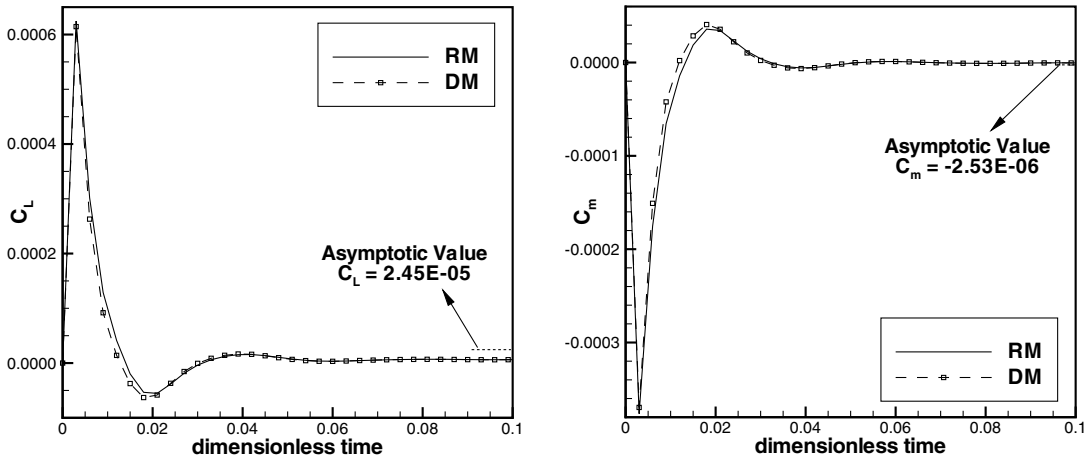

a) C_l time history b) C_m time history

Fig. 21 Initial part of the response of a NACA 0012 airfoil at $M_\infty = 0.8$ and $\alpha_0 = 0$ to a DS in pitch. Comparison between DM and RM simulations.

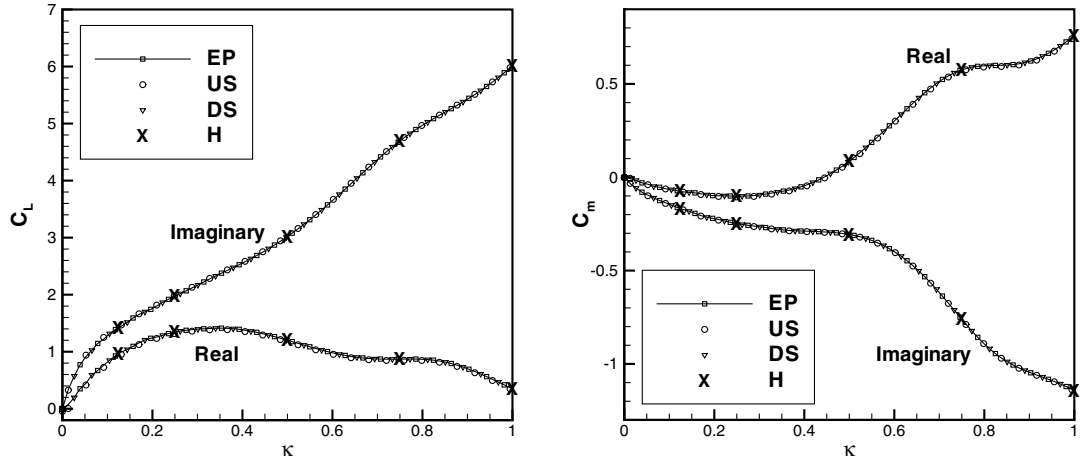

a) C_l frequency domain response b) C_m frequency domain response

Fig. 22 Low reduced frequency impulsive responses of a NACA 0012 airfoil at $M_\infty = 0.8$ and $\alpha_0 = 0$ to inputs in plunge. Simulations consider a rigid mesh.

the small differences observed in the time responses are responsible for the frequency domain discrepancies seen in the preceding section. Furthermore, it is evident that all the approaches applied to acquire the elementary aerodynamic solutions generate the same impulsive results when the RM algorithm is considered. Such results confirm the reasoning that the mesh deformation is responsible for the differences observed in Figs. 12 and 13. Therefore, this is a demonstration that it is possible to numerically obtain direct

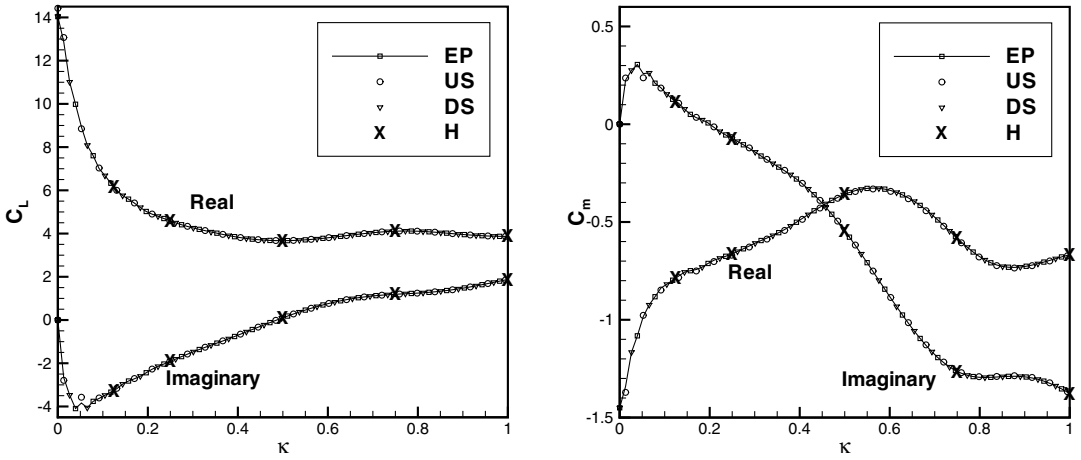

a) C_l frequency domain response b) C_m frequency domain response

Fig. 23 Low reduced frequency impulsive responses of a NACA 0012 airfoil at $M_\infty = 0.8$ and $\alpha_0 = 0$ to inputs in pitch. Simulations consider a rigid mesh.

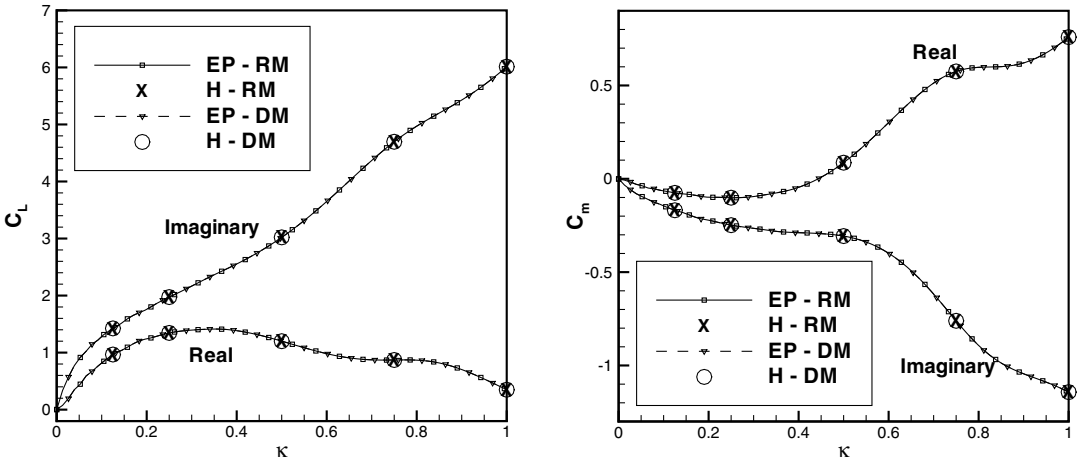

a) C_l frequency domain response b) C_m frequency domain response

Fig. 24 Low reduced frequency impulsive response of a NACA 0012 airfoil at $M_\infty = 0.8$ and $\alpha_0 = 0$ to an EP in plunge. Comparison between DM and RM simulations.

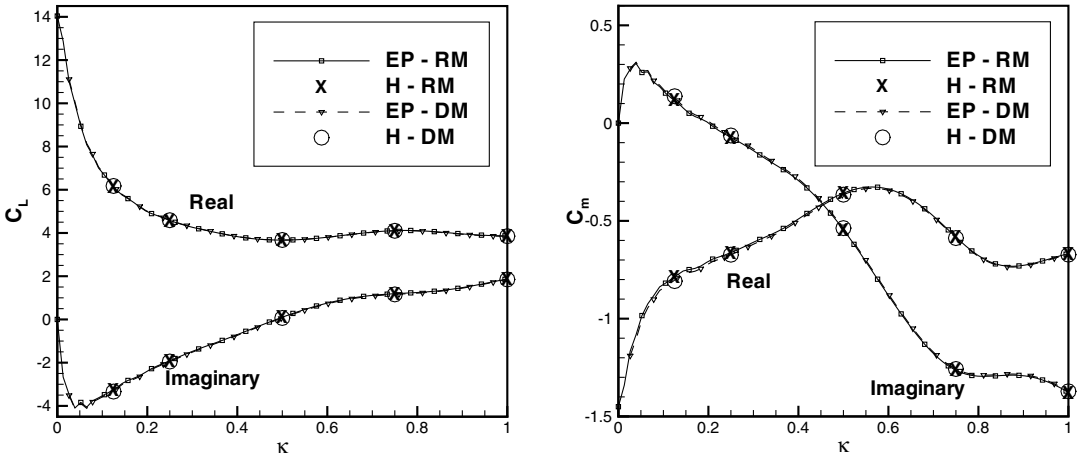

a) C_l frequency domain response b) C_m frequency domain response

Fig. 25 Low reduced frequency impulsive response of a NACA 0012 airfoil at $M_\infty = 0.8$ and $\alpha_0 = 0$ to an EP in pitch. Comparison between DM and RM simulations.

aerodynamic responses to unit sample and discrete step inputs. Moreover, as presented before, these responses are exact, and not mere approximations, at least within the numerical scheme and discrete-time contexts.

Additionally, Figs. 24 and 25 show comparisons of the impulsive frequency domain responses obtained with deformable and rigid mesh algorithms for the EP cases. As expected from the time domain responses, these results also agree in the frequency domain. This

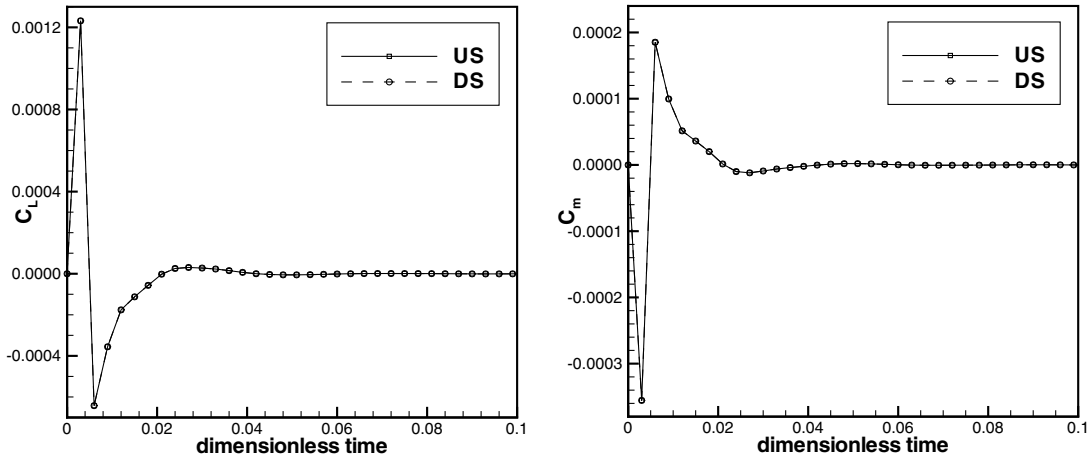

a) C_l time history b) C_m time history

Fig. 26 Initial part of the response of a NACA 0012 airfoil at $M_\infty = 0.8$ and $\alpha_0 = 0$ to a US in plunge. Comparison between the responses acquired directly (US) and through the use of discrete step (DS) responses. Simulations consider a rigid mesh.

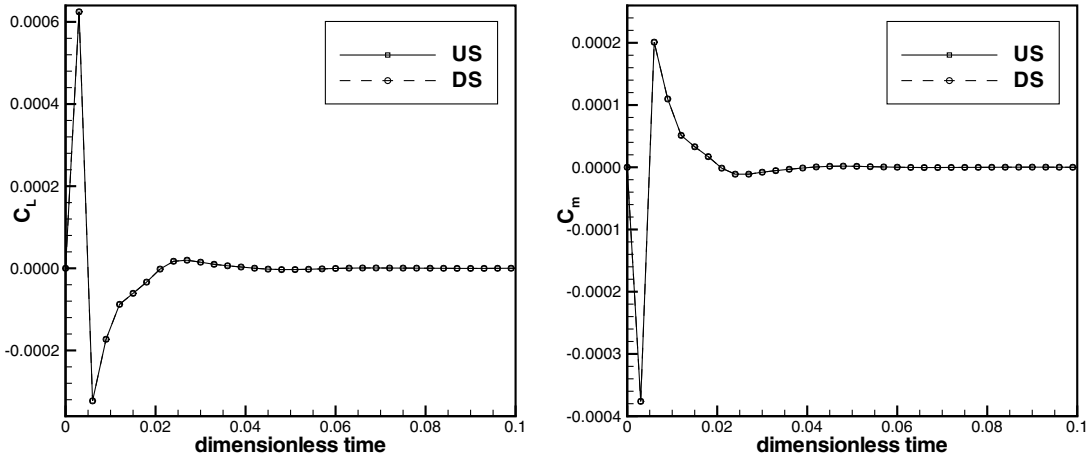

a) C_l time history b) C_m time history

Fig. 27 Initial part of the response of a NACA 0012 airfoil at $M_\infty = 0.8$ and $\alpha_0 = 0$ to a US in pitch. Comparison between the responses acquired directly (US) and through the use of discrete step (DS) responses. Simulations consider a rigid mesh.

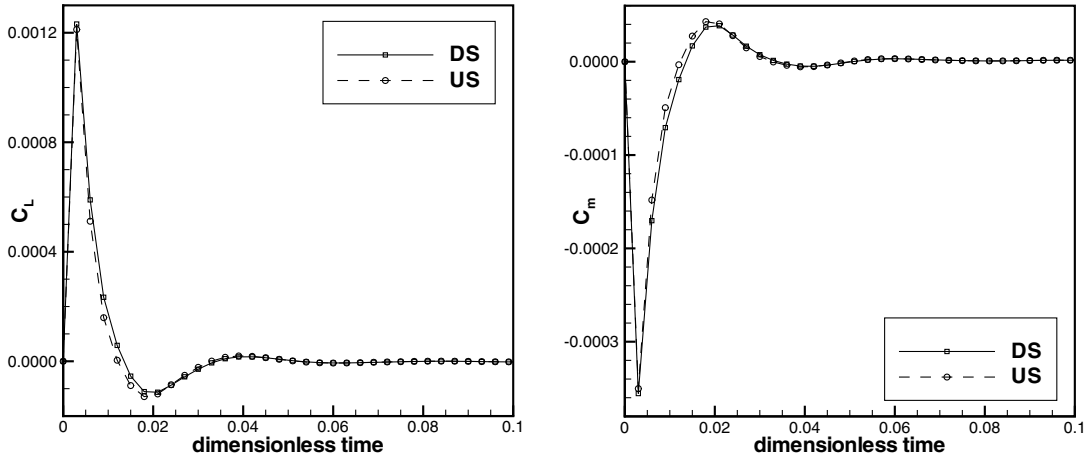

a) C_l time history b) C_m time history

Fig. 28 Initial part of the response of a NACA 0012 airfoil at $M_\infty = 0.8$ and $\alpha_0 = 0$ to a DS in plunge. Comparison between the responses acquired directly (DS) and through convolution (US). Simulations consider a rigid mesh.

shows that the use of smooth motions is not affected by the mesh deformation effects, and, hence, the smooth pulse technique is a more robust procedure than directly obtaining unit sample or discrete step responses.

The correspondence among the different solutions can also be verified in the time domain. For example, as presented in [17], the unit sample responses can be obtained with the backward difference of the corresponding discrete step solutions, as indicated in Eq. (5),

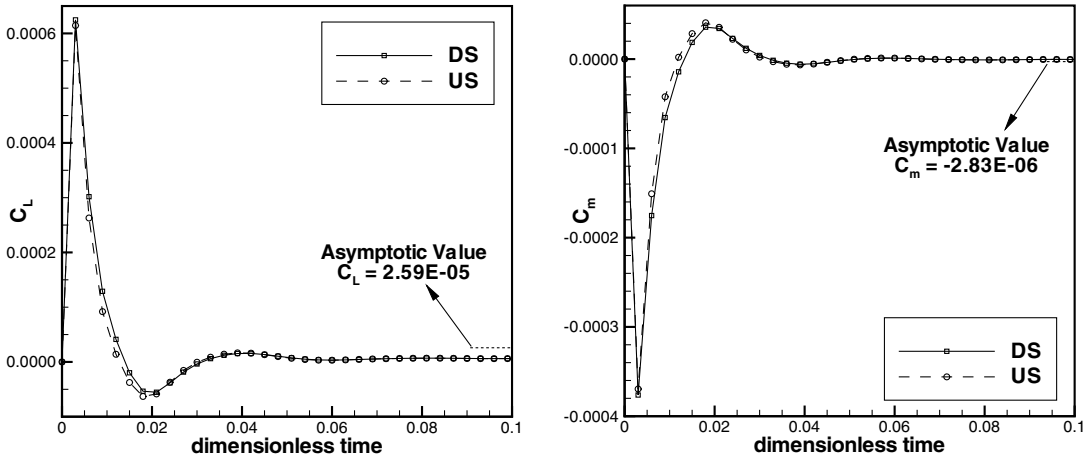

a) C_l time history b) C_m time history

Fig. 29 Initial part of the response of a NACA 0012 airfoil at $M_\infty = 0.8$ and $\alpha_0 = 0$ to a DS in pitch. Comparison between the responses acquired directly (DS) and through convolution (US). Simulations consider a rigid mesh.

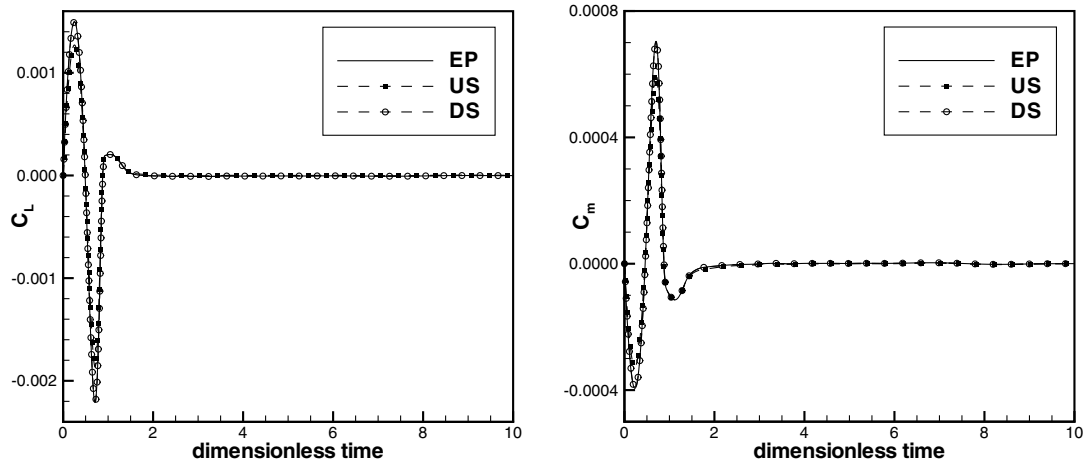

a) C_l time history b) C_m time history

Fig. 30 Initial part of the response of a NACA 0012 airfoil at $M_\infty = 0.8$ and $\alpha_0 = 0$ to an EP in plunge. Comparison between the responses acquired directly (EP) and through convolution (US and DS). Simulations consider a rigid mesh.

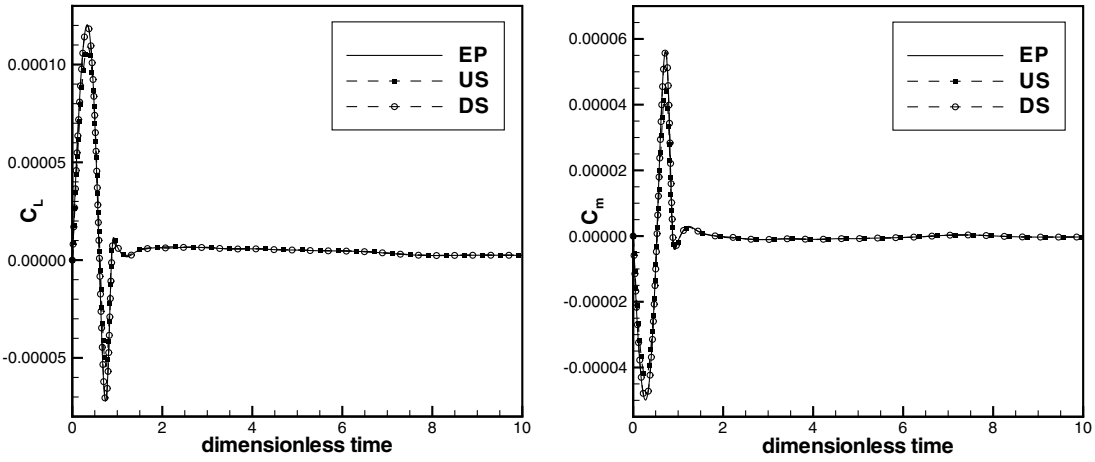

a) C_l time history b) C_m time history

Fig. 31 Initial part of the response of a NACA 0012 airfoil at $M_\infty = 0.8$ and $\alpha_0 = 0$ to an EP in pitch. Comparison between the responses acquired directly (EP) and through convolution (US and DS). Simulations consider a rigid mesh.

Table 1 Amplitude values used for each input

Motion	Mode	High amplitude (HA)	Low amplitude (LA)
EP	Plunge	$0.01c$	$0.0001c$
EP	Pitch	0.1 deg	0.001 deg
US	Plunge	$0.0001c$	$0.000001c$
US	Pitch	0.01 deg	0.0001 deg
DS	Plunge	$0.0001c$	$0.000001c$
DS	Pitch	0.01 deg	0.0001 deg

and shown in Figs. 26 and 27. On the other hand, the discrete step responses can be reproduced by a convolution sum between the unit sample ones and the DS sequence, as demonstrated in Figs. 28 and 29. The asymptotic values shown in Fig. 29 corresponds to the solutions obtained by convolution. As one can observe, the DS response evaluated by convolution presents small differences in the initial values when compared with the one directly obtained, but the asymptotic solutions are very close in both cases (see Fig. 21). This suggests that these time solutions differ only in the high-frequency content.

Although it may seem that the same unit sample responses can be obtained from the exponentially shaped solutions through the inverse discrete Fourier transform of the frequency domain response given in Figs. 22 and 23, this is not possible. A unit sample response contains information about a large frequency range, which is only limited by numerical factors such as time step and mesh resolution, whereas a smooth input is not able to properly excite higher frequency values. Therefore, although both responses are coincident in a certain frequency range, they are not equivalent, and this is reflected in the time domain. Nevertheless, the exponentially shaped responses can be reproduced with convolution sums, either from the unit sample or discrete step responses, as presented in Figs. 30 and 31. The direct EP response coincides with the one obtained by convolution with the DS data. On the other hand, it presents some small differences with the other convolution response in the initial portion of the time response. The small errors present, when representing other solutions from the convolution of the US response, demonstrate the numerical difficulty of obtaining the unit sample response through direct application of a US input.

D. Motion Amplitude and Steady-State Convergence

Raveh [10] showed how numerical parameters can influence the direct determination of aerodynamic unit sample and discrete step responses. In an attempt to contribute with such discussion, the present authors present what their experience has revealed about two important factors: motion amplitude and steady-state convergence. To start with, it is relevant to notice that the motion amplitude, as explained in [10], is related to the perturbation velocity imposed to the flow. Therefore, for a fixed time step, the lower the input amplitude, the smaller the perturbation. As every numerical scheme

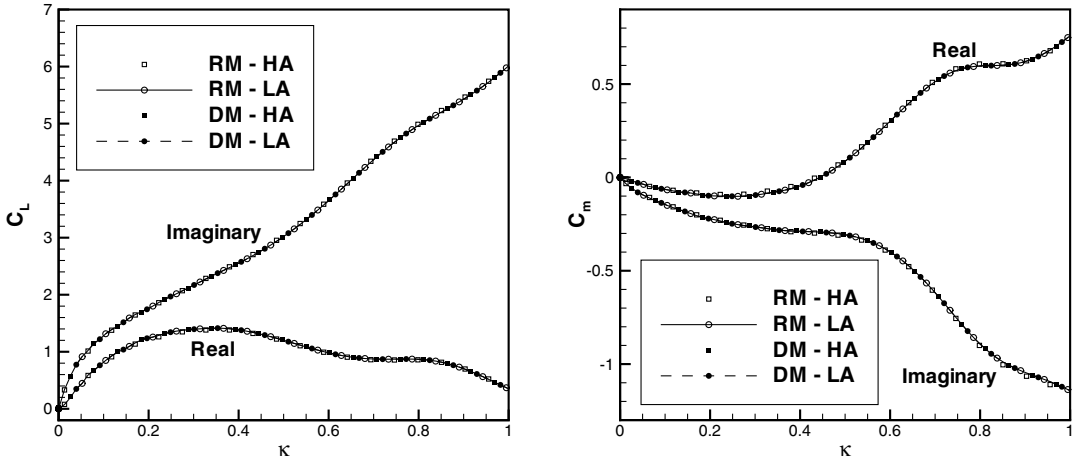

a) C_l frequency domain response b) C_m frequency domain response

Fig. 32 Low reduced frequency impulsive response of a NACA 0012 airfoil at $M_\infty = 0.8$ and $\alpha_0 = 0$ to an EP in plunge. Comparisons between low-amplitude (LA) and high-ampltude (HA) motions.

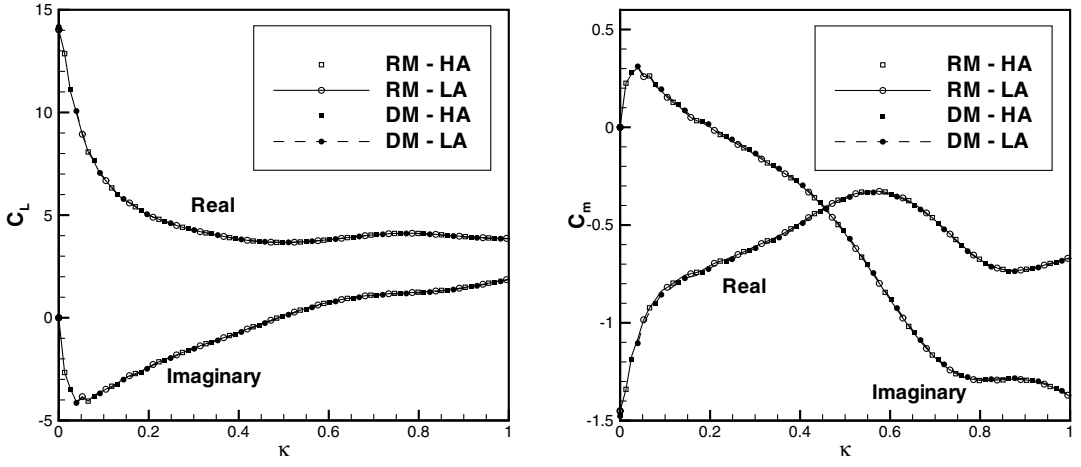

a) C_l frequency domain response b) C_m frequency domain response

Fig. 33 Low reduced frequency impulsive response of a NACA 0012 airfoil at $M_\infty = 0.8$ and $\alpha_0 = 0$ to an EP in pitch. Comparisons between LA and HA motions.

has a maximum characteristic propagation velocity it can resolve, if the perturbation velocity exceeds this value, the numerical solution contains errors. Moreover, because the preceding results showed the rigid mesh algorithm to be more robust for the cases considered here, all the following comparisons are based on such approach, except where specifically indicated otherwise. Hence, the NACA 0012 airfoil, at the same conditions previously presented, is submitted to the three motions, EP, US, and DS, with two different amplitudes for

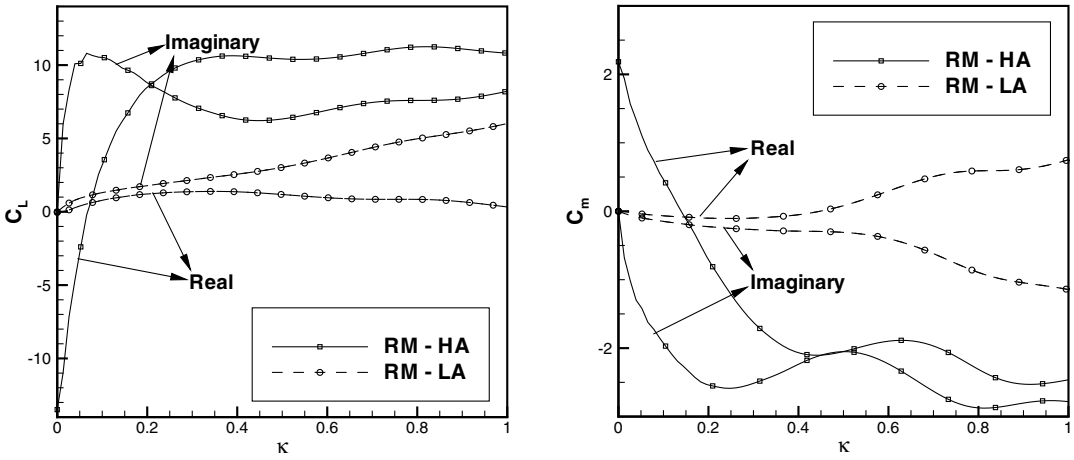

a) C_l frequency domain response b) C_m frequency domain response

Fig. 34 Low reduced frequency impulsive response of a NACA 0012 airfoil at $M_\infty = 0.8$ and $\alpha_0 = 0$ to a US in plunge. Comparisons between LA and HA motions.

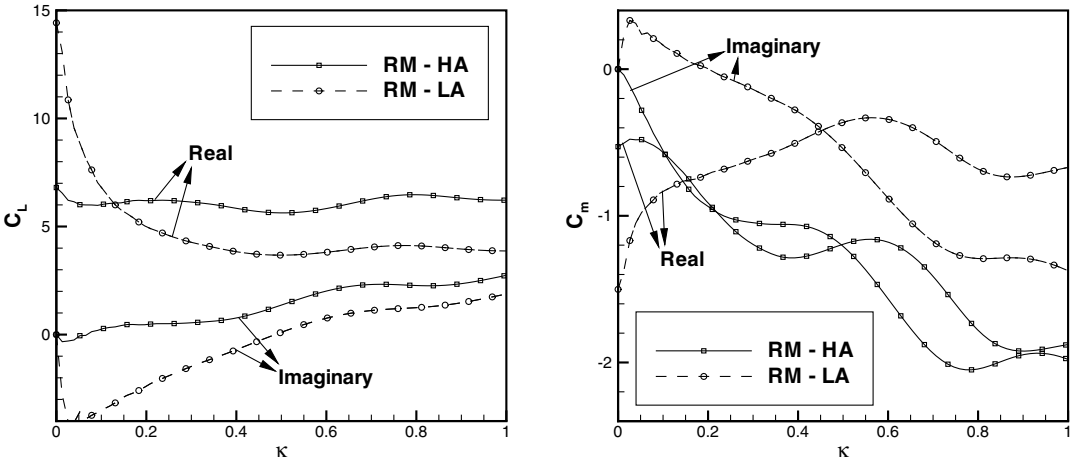

a) C_l frequency domain response b) C_m frequency domain response

Fig. 35 Low reduced frequency impulsive response of a NACA 0012 airfoil at $M_\infty = 0.8$ and $\alpha_0 = 0$ to a US in pitch. Comparisons between LA and HA motions.

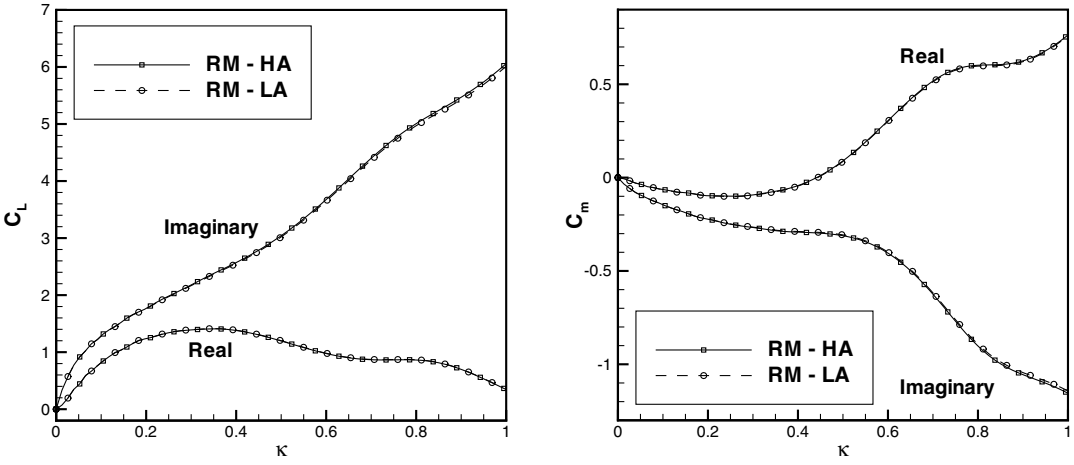

a) C_l frequency domain response b) C_m frequency domain response

Fig. 36 Low reduced frequency impulsive response of a NACA 0012 airfoil at $M_\infty = 0.8$ and $\alpha_0 = 0$ to a DS in plunge. Comparisons between LA and HA motions.

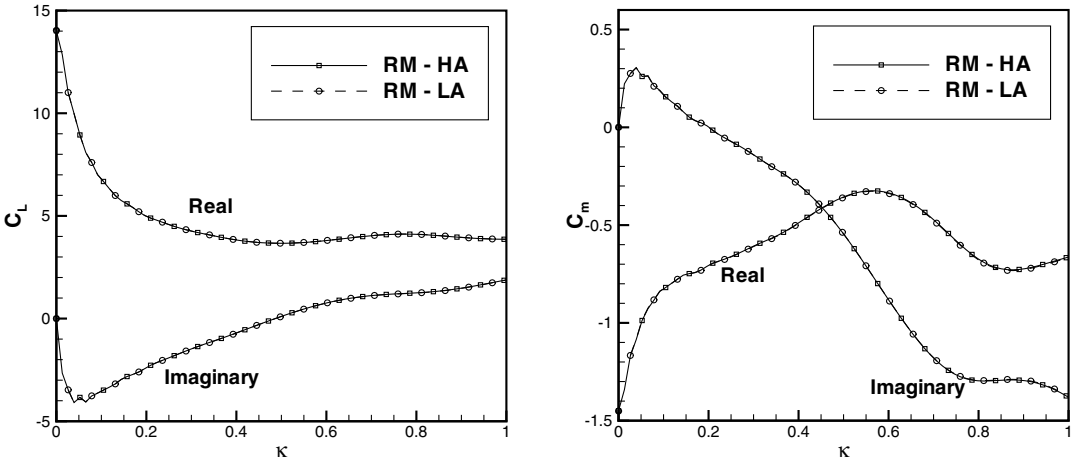

a) C_l frequency domain response b) C_m frequency domain response

Fig. 37 Low reduced frequency impulsive response of a NACA 0012 airfoil at $M_\infty = 0.8$ and $\alpha_0 = 0$ to a DS in pitch. Comparisons between LA and HA motions.

each case. Henceforth, these motions are designated as low amplitude (LA) and high amplitude (HA). The values used for each input are described in Table 1. One should notice that the low-amplitude values are always 2 orders of magnitude lower than the corresponding high-amplitude ones.

As this section is devoted to comparisons, rather than discussing the individual solutions, only frequency domain responses are presented. Thus, Figs. 32–37 present the results for the high- and low-amplitude inputs in both plunge and pitch modes. These results corroborate what Raveh [10] stated about directly obtaining aerodynamic unit sample responses. The solution to a US motion is much more influenced by the input amplitude than the other types of motion considered. Actually, solutions to the other motions behaved practically indifferent to the input amplitude, at least for the range considered. This is already expected from the EP because it is a smooth motion. However, the robustness of the DS response in relation to the input amplitude is quite surprising to the authors. Raveh [10] attributes this difference between US and DS behaviors to the extent of the initial perturbation. The DS motion imposes a high perturbation velocity in the first time step, and then it no longer disturbs the flow. On the other hand, besides this first step perturbation, the US motion imposes exactly the same perturbation, but in opposite direction, in the second time step. This results in a much higher disturbance that has to be resolved by the numerical scheme.

To explore the influence of the steady-state convergence, it is important to establish a variable which is representative of such parameter. The residue may be interpreted as a measurement of convergence of the steady-state solution. For the ith control volume, the residue is defined as

$$RES_i = -(C_i - D_i) \tag{74}$$

Consequently, at a determined iteration, each control volume has its own residue. Moreover, this quantity is actually a four-component vector rather than a single variable. However, the density component of such vector is the one that presents the slowest convergence behavior, and, therefore, it is used as the indicator of solution convergence. Therefore, henceforth, the present authors use the term residue to designate the maximum value of the individual density component of the residue throughout the entire computational domain.

The influence of the steady-state convergence is easily understood if one considers what happens if a steady-state is simulated in a time-accurate fashion for a few more time steps, without any perturbation. Two cases are considered as a means of showing the influence of steady-state convergence in the unsteady responses. The first one, designated as high residue (HR), represents a poorly converged steady state, with convergence residue of the order of 1×10^{-6}. The other, called low residue (LR), indicates a well-converged case, with convergence residue of the order of 1×10^{-10}. Figure 38 shows the residue change along the iterations for both cases when no perturbation is imposed.

This residue change is reflected in the aerodynamic response. Figure 39 presents the C_ℓ and C_m fluctuations that occur for the same situation, that is, for time-accurate iterations with no perturbation. Actually, the plotted values are the difference between the instantaneous response and the initial solution. This is why some of the responses do not tend to zero, as one could expect. It is clear that these coefficients undergo small variations during the considered time. However, despite being small, these variations may be of the same order of the real unsteady aerodynamic response when the input amplitude is very small, as in the unit sample case. This is especially relevant in the low-frequency range, which is determined by the asymptotic values of the time history of the aerodynamic response.

With the objective of evaluating the influence of the steady-state convergence in the cases considered in the present work, the test case in question is simulated with the low-amplitude EP, US, and DS excitations, but with different values of initial residue. The responses for these cases are shown in Figs. 40–45.

As Figs. 40, 41, 44, and 45 show, the steady-state convergence has no influence in the unsteady solutions obtained with the EP and DS inputs. However, this does not mean that, in such cases, the steady-state solution is not important for the unsteady calculations. The fact is

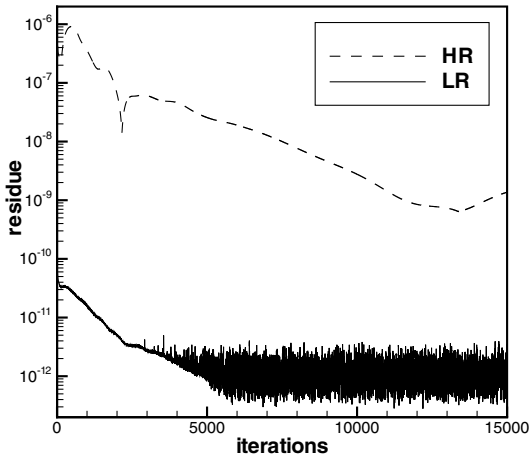

Fig. 38 Residue change for a NACA 0012 airfoil at $M_\infty = 0.8$ and $\alpha_0 = 0$ with no disturbance. Comparisons between low- (LR) and high-residue (HR) initial states.

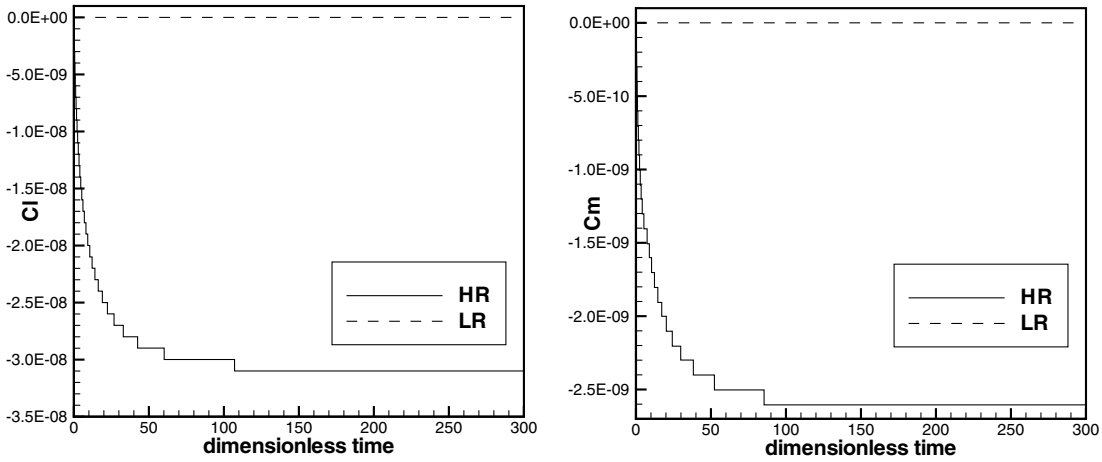

a) C_l time history b) C_m time history

Fig. 39 C_ℓ and C_m fluctuations for a NACA 0012 airfoil at $M_\infty = 0.8$ and $\alpha_0 = 0$ with no disturbance. Comparisons between LR and HR initial states.

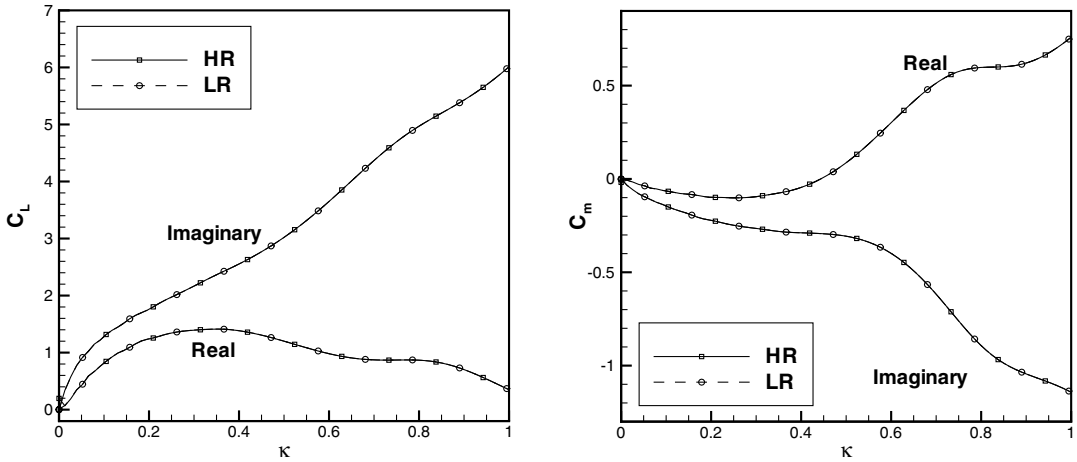

a) C_l frequency domain response b) C_m frequency domain response

Fig. 40 Low reduced frequency impulsive response of a NACA 0012 airfoil at $M_\infty = 0.8$ and $\alpha_0 = 0$ to an EP in plunge. Comparisons between LR and HR initial states.

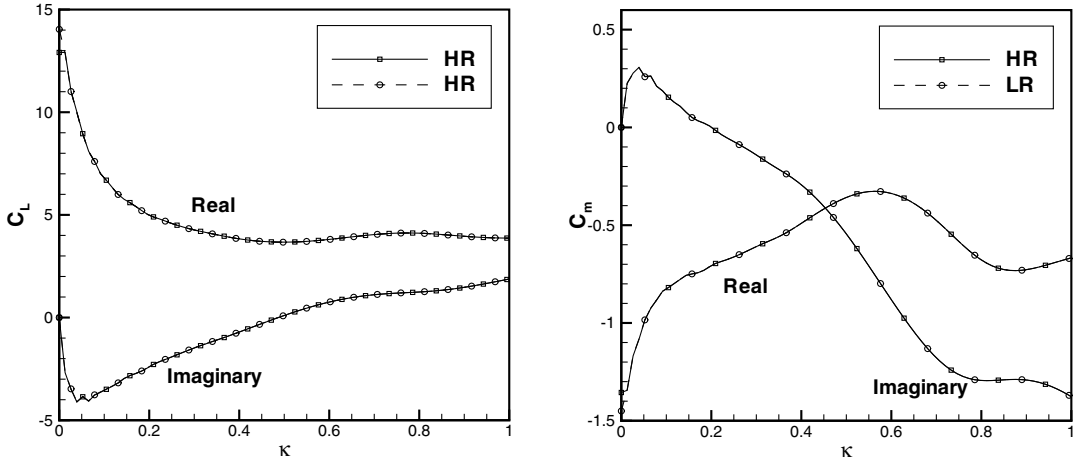

a) C_l frequency domain response b) C_m frequency domain response

Fig. 41 Low reduced frequency impulsive response of a NACA 0012 airfoil at $M_\infty = 0.8$ and $\alpha_0 = 0$ to an EP in pitch. Comparisons between LR and HR initial states.

that the residue value designated as HR is not actually too high. A convergence residue of the order of 1×10^{-6} is many times acceptable for steady-state calculations. On the other hand, Figs. 42 and 43 show that the US simulations are tremendously affected by the steady-state convergence. In this case, a much more restrict convergence criterion is required, such as the LR value. Furthermore, it is also important to notice that all the other results contained in the present paper are obtained starting from the low-residue steady-state cases.

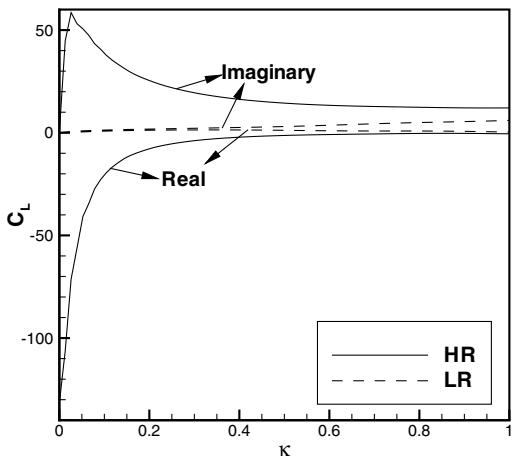

a) C_l frequency domain response

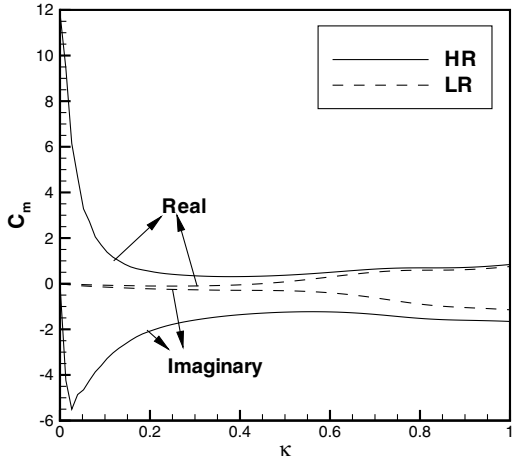

b) C_m frequency domain response

Fig. 42 Low reduced frequency impulsive response of a NACA 0012 airfoil at $M_\infty = 0.8$ and $\alpha_0 = 0$ to a US in plunge. Comparisons between LR and HR initial states.

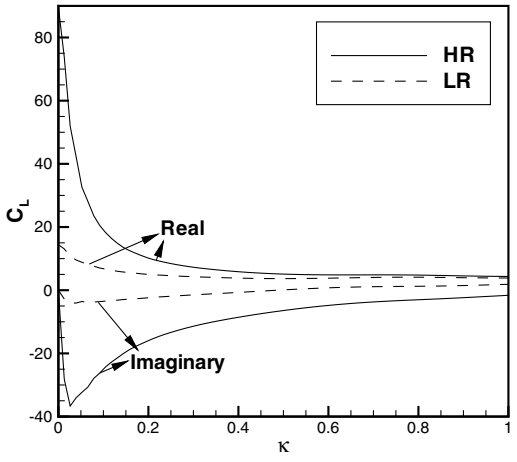

a) C_l frequency domain response

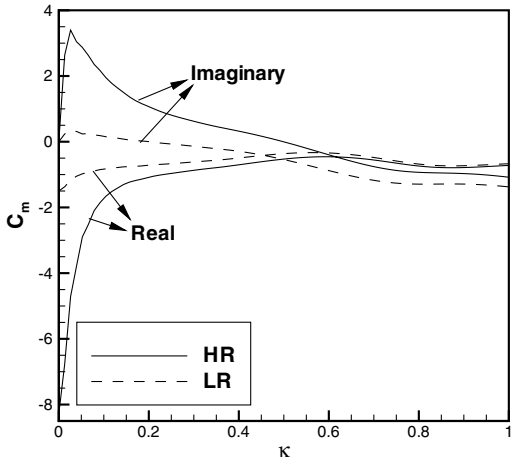

b) C_m frequency domain response

Fig. 43 Low reduced frequency impulsive response of a NACA 0012 airfoil at $M_\infty = 0.8$ and $\alpha_0 = 0$ to a US in pitch. Comparisons between LR and HR initial states.

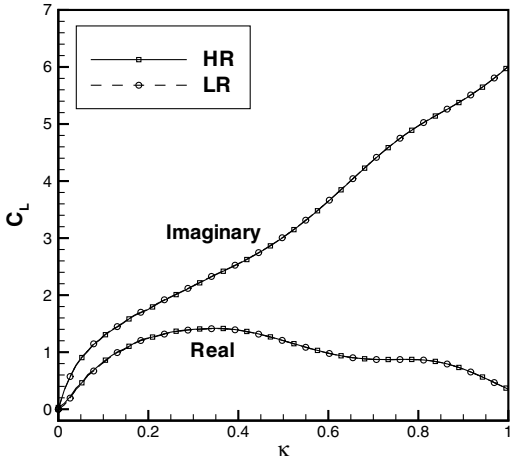

a) C_l frequency domain response

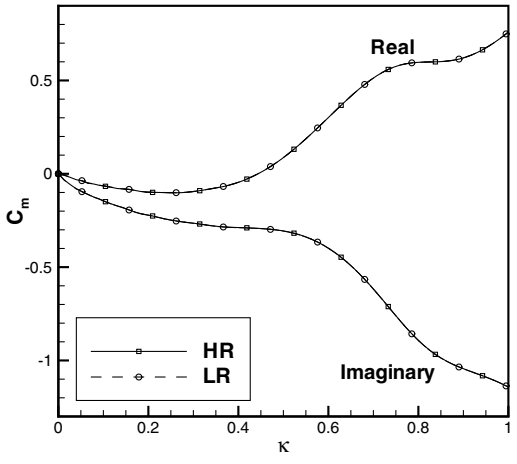

b) C_m frequency domain response

Fig. 44 Low reduced frequency impulsive response of a NACA 0012 airfoil at $M_\infty = 0.8$ and $\alpha_0 = 0$ to a DS in plunge. Comparisons between LR and HR initial states.

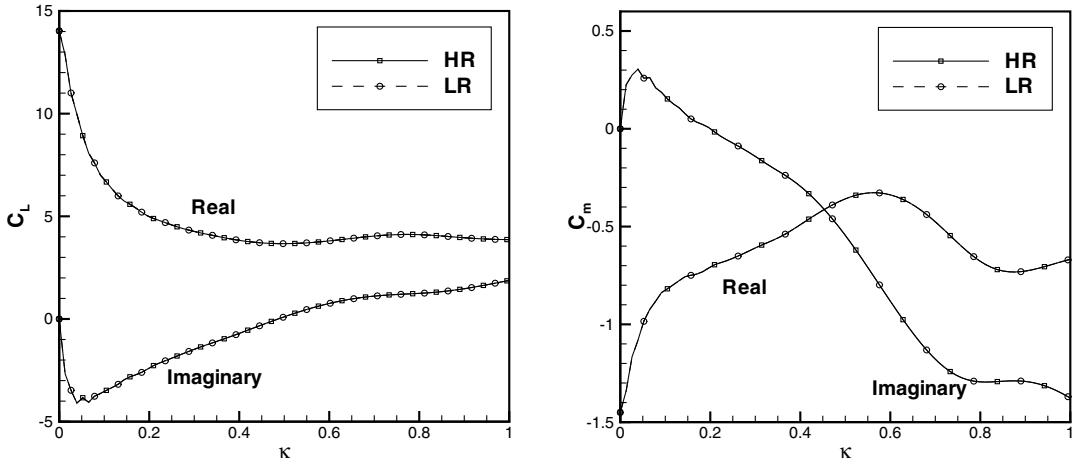

a) C_l frequency domain response

b) C_m frequency domain response

Fig. 45 Low reduced frequency impulsive response of a NACA 0012 airfoil at $M_\infty = 0.8$ and $\alpha_0 = 0$ to a DS in pitch. Comparisons between LR and HR initial states.

VI. Conclusions

The authors present a thorough analysis of the application of a CFD solver for obtaining impulsive and indicial aerodynamic responses. First of all, it is demonstrated that, under the new discrete-time interpretation of CFD solvers, it is possible to obtain impulsive and indicial aerodynamic responses with the direct use of unit sample and discrete step sequences as inputs. Furthermore, according to such interpretation, these responses are not approximations to the expected continuous-time impulsive and indicial solutions, but they are the formal elementary solutions for the discrete-time aerodynamic system represented by the discretized equations. However, direct calculation of such responses can lead to many numerical difficulties. The authors show that the capability of the CFD code of solving certain disturbance velocities is closely related to the maximum perturbation that can be imposed on the flowfield without compromising the unsteady responses. Moreover, the relevance of the steady-state convergence in the subsequent unsteady calculations is also presented. It is important to emphasize that the conceptual closure of the proper calculation of aerodynamic elementary solutions is relevant in many areas, in particular in the development of reduced-order models for aeroservoelastic control laws.

The authors also show the correctness of the use of smooth input functions to determine the impulsive aerodynamic responses in certain frequency ranges. In this context, an important conclusion of the present work is that the different manners of obtaining aerodynamic elementary solutions are equivalent. Additionally, the application of smooth motions has been shown to yield much more robust numerical behavior for the aerodynamic responses.

Although the test case considered throughout this paper concerns a single numerical scheme applied to a particular aerodynamic configuration, the authors' experience and the arguments contained herein indicate that there are no restrictions in expanding the present conclusions to more general situations. Therefore, the authors hope to have made a contribution to the understanding of the use of CFD solvers as reliable sources of aerodynamic unsteady responses.

Acknowledgments

The authors gratefully acknowledge the partial support for this research provided by Conselho Nacional de Desenvolvimento Científico e Tecnológico, CNPq, under the Integrated Project Research Grants No. 501200/2003-7 and 312064/2006-3. This work is also supported by Fundação de Amparo à Pesquisa do Estado de São Paulo (FAPESP) through a Master of Science Scholarship for the first author according to FAPESP Process No. 04/11200-1. Further support from FAPESP is provided through Process No. 04/16064-9. Finally, the authors thank Carlos F. C. Simões for valuable discussions, which were extremely important for the achievement of the present successful results.

References

[1] Bisplinghoff, H. L., Ashley, H. L., and Halfman, R. L., *Aeroelasticity*, Adison Wesley Longman, Cambridge, MA, 1955.

[2] Lin, J., and Iliff, K. W., "Aerodynamic Lift and Moment Calculations Using a Closed-Form Solution of the Possio Equation," NASA TM-2000-209019, April 2000.

[3] Tijdeman, H., "Investigation of the Transonic Flow Around Oscillating Airfoils," National Aerospace Laboratory, NLR-TR-77090U, 1977.

[4] Beam, R. M., and Warming, R. F., "Numerical Calculations of Two-Dimensional, Unsteady Transonic Flows with Circulation," NASA TN D-7605, Feb. 1974.

[5] Traci, R. M., Albano, E. D., and Farr, J. L., "Small Disturbance Transonic Flows About Oscillating Airfoils and Planar Wings," Air Force Flight Dynamics Laboratory, AFFDL-TR-75-100, Aug. 1975.

[6] Ballhaus, W. F., and Goorjian, P. M., "Computation of Unsteady Transonic Flows by the Indicial Method," *AIAA Journal*, Vol. 16, No. 2, Feb. 1978, pp. 117–124.

[7] Yang, T. Y., Guruswamy, P., and Striz, A. G., "Application of Transonic Codes to Flutter Analysis of Conventional and Supercritical Airfoils," *Journal of Aircraft*, Vol. 19, No. 3, March 1982, pp. 211–220.

[8] Ashley, H., "Role of Shocks in the "Sub-Transonic" Flutter Phenomenon," *Journal of Aircraft*, Vol. 17, No. 3, March 1980, pp. 187–197.

[9] Hirsch, C., *Numerical Computation of Internal and External Flows: Fundamentals of Numerical Discretization*, Vol. 1, Wiley, Chichester, England, 1992.

[10] Raveh, D. E., "Reduced-Order Models for Nonlinear Unsteady Aerodynamics," *AIAA Journal*, Vol. 39, No. 8, Aug. 2001, pp. 1417–1429.

[11] Bakhle, M. A., Mahjan, A. J., Keith, T. G., and Stefko, G. L., "Cascade Flutter Analysis with Transient Response Aerodynamics," *Computers and Structures*, Vol. 41, No. 5, 1991, pp. 1073–1085. doi:10.1016/0045-7949(91)90302-3

[12] Davies, B., *Applied Mathematical Sciences: Integral Transforms and Their Applications*, Vol. 25, Springer–Verlag, New York, 1978.

[13] Oliveira, L. C., "A State-Space Aeroelastic Analysis Methodology Using Computational Aerodynamics Techniques," Master's Thesis, Instituto Tecnológico de Aeronáutica, São José dos Campos, SP, Brazil, Aug. 1993 (in Portuguese).

[14] Silva, W. A., "Identification of Linear and Nonlinear Aerodynamic Impulse Responses Using Digital Filter Techniques," NASA Langley Research Center, NASA TM-112872, Aug. 1997.

[15] Oppenheim, A. V., and Schafer, R. W., *Discrete-Time Signal Processing*, Prentice–Hall, Englewood Cliffs, NJ, 1989.

[16] Davies, D., and Salmond, D. J., "Indicial Approach to Harmonic Perturbations in Transonic Flow," *AIAA Journal*, Vol. 18, No. 8, Aug. 1980, pp. 1012–1014.

[17] Marques, A. N., and Azevedo, J. L. F., "Application of CFD-Based Unsteady Forces for Efficient Aeroelastic Stability Analyses," AIAA Paper No. 2006-0250, Jan. 2006.

[18] Azevedo, J. L. F., "Euler Solutions of Transonic Nozzle Flows," *Proceedings of the 3rd National Meeting on Thermal Sciences: III ENCIT*, ABCM, Rio de Janeiro, Brazil, Dec. 1990, pp. 243–248.

[19] Azevedo, J. L. F., Fico, N. G. C. R., Jr., and Ortega, M. A., "Two-Dimensional and Axisymmetric Nozzle Flow Computation Using the Euler Equations," *Journal of the Brazilian Society of Mechanical Sciences*

and Engineering, Vol. 17, No. 2, April–June 1995, pp. 147–170.

[20] Azevedo, J. L. F., Strauss, D., and Ferrari, M. A. S., "Viscous Multiblock Simulations of Axisymmetric Launch Vehicle Flows," *Journal of Spacecraft and Rockets*, Vol. 36, No. 4, July–Aug. 1999, pp. 489–498.

[21] Bigarelli, E. D. V., Mello, O. A. F., and Azevedo, J. L. F., "Three Dimensional Flow Simulations for Typical Launch Vehicles at Angle of Attack," *Proceedings of the 15th Brazilian Congress on Mechanical Engineering: COBEM 1999* [CD-ROM], ABCM, Rio de Janeiro, Brazil, Nov. 1999.

[22] Simões, C. F. C., and Azevedo, J. L. F., "The Influence of Numerical Parameters on Unsteady Airfoil Inviscid Flow Simulations Using Unstructured Dynamic Meshes," *Proceedings of the 15th Brazilian Congress of Mechanical Engineering—COBEM 1999* [CD-ROM], ABCM, Rio de Janeiro, Brazil, Nov. 1999.

[23] Bigarelli, E. D. V., and Azevedo, J. L. F., "On Turbulence Models for 3-D Aerospace Applications,"*Proceedings of the 9th Brazilian Congress of Thermal Engineering and Sciences* [CD-ROM], ABCM, Rio de Janiero, Brazil, Oct. 2002; also ABCM Paper CIT02-0341.

[24] Marques, A. N., "Simulation of Unsteady Aerospace Flows Using Unstructured Meshes," Graduation Project, Instituto Tecnológico de Aeronáutica, São José dos Campos, SP, Brazil, Dec. 2004 (in Portuguese).

[25] Brigham, E. O., *The Fast Fourier Transform and Its Applications*, Prentice–Hall, Englewood Cliffs, NJ, 1988.

[26] Mohr, R. W., Batina, J. T., and Yang, H. T. Y., "Mach Number Effects on Transonic Aeroelastic Forces and Flutter Characteristics," *Journal of Aircraft*, Vol. 26, No. 11, Nov. 1989, pp. 1038–1046.

[27] Silva, W. A., "Application of Nonlinear Systems Theory to Transonic Unsteady Aerodynamic Responses," *Journal of Aircraft*, Vol. 30, No. 5, Sept.–Oct. 1993, pp. 660–668.

[28] Silva, W. A., "Extension of a Nonlinear Systems Theory to General-Frequency Unsteady Transonic Aerodynamic Responses," AIAA Paper No. 93-1590, April 1993.

[29] Silva, W. A., and Raveh, D. E., "Development of Unsteady Aerodynamic State-Space Models from CFD-Based Pulse Responses," AIAA Paper No. 2001-1213, April 2001.

[30] Jameson, A., and Mavriplis, D., "Finite Volume Solution of the Two-Dimensional Euler Equations on a Regular Triangular Mesh," *AIAA Journal*, Vol. 24, No. 4, April 1986, pp. 611–618.

[31] Pulliam, T. H., "Artificial Dissipation Models for the Euler Equations," *AIAA Journal*, Vol. 24, No. 12, Dec. 1986, pp. 1931–1940.

[32] Fletcher, C. A. J., *Computational Techniques for Fluid Dinamics: Fundamental and General Techniques*, Vol. 1, Springer–Verlag, Berlin, 1988.

[33] Hirsch, C., *Numerical Computation of Internal and External Flows: Computational Methods for Inviscid and Viscous Flows*, Vol. 2, Wiley, Chichester, England, 1992.

[34] Jameson, A., Schmidt, W., and Turkel, E., "Numerical Solution of the Euler Equations by Finite Volume Methods Using Runge–Kutta Time-Stepping Schemes," AIAA Paper No. 81-1259, June 1981.

[35] Batina, J. T., "Unsteady Euler Airfoil Solutions Using Unstructured Dynamic Meshes," AIAA Paper No. 89-0115, Jan. 1989.

[36] Mavriplis, D. J., "Accurate Multigrid Solution of the Euler Equations on Unstructured and Adaptative Meshes," *AIAA Journal*, Vol. 28, No. 2, Feb. 1990, pp. 213–221.

[37] Jameson, A., and Baker, T. J., "Solution of the Euler Equation for Complex Configurations," AIAA Paper No. 83-1929, July 1983.

[38] Jameson, A., and Baker, T. J., "Improvements to the Aircraft Euler Method," AIAA Paper No. 87-0452, Jan. 1987.

[39] Thomas, P. D., and Lombard, C. K., "Geometric Conservation Law and Its Application to Flow Computations on Moving Grids," *AIAA Journal*, Vol. 17, No. 10, Oct. 1979, pp. 1030–1037.

[40] Azevedo, J. L. F., "On the Development of Unstructured Grid Finite Volume Solvers for High Speed Flows," Report NT-075-ASE-N/92, Instituto de Aeronáutica e Espaço, Dec. 1992.

[41] Kroll, N., and Jain, R. K., "Solutions of the Two-Dimensional Euler Equations: Experience with a Finite Volume Code," Deutsche Forschungs und Versuchsanstalt für Luft und Raumfahrt Research Rept. DFVLR-FB 87/41, Braunschweig, Germany, Jan. 1987.

[42] McDevitt, J. B., and Okuno, A. F., "Static and Dynamic Pressure Measurments on a NACA 0012 Airfoil in the Ames High Reynolds Number Facility," NASA Ames Research Center, NASA TP-2485, Feb. 1985.

[43] Rausch, R. D., Batina, J. T., and Yang, H. T. Y., "Euler Flutter Analysis of Airfoils Using Unstructured Dynamic Meshes," *Journal of Aircraft*, Vol. 27, No. 5, May 1990, pp. 436–443.